A new insight ~~of~~ into the vertical differences ~~of~~ in NO_2 heterogeneous reaction to produce HONO over inland and marginal seas

Chengzhi Xing[a], Shiqi Xu[g], Yuhang Song[b], Cheng Liu[b,a,c,d,*], Yuhan Liu[f], Keding Lu[e,*], Wei Tan[a], Chengxin Zhang[b], Qihou Hu[a], Shanshan Wang[i], Hongyu Wu[h], and Hua Lin[h]

[a] Key Lab of Environmental Optics & Technology, Anhui Institute of Optics and Fine Mechanics, Hefei Institutes of Physical Science, Chinese Academy of Sciences, Hefei 230031, China

[b] Department of Precision Machinery and Precision Instrumentation, University of Science and Technology of China, Hefei, 230026, China

[c] Center for Excellence in Regional Atmospheric Environment, Institute of Urban Environment, Chinese Academy of Sciences, Xiamen, 361021, China

[d] Key Laboratory of Precision Scientific Instrumentation of Anhui Higher Education Institutes, University of Science and Technology of China, Hefei, 230026, China

[e] State Key Joint Laboratory of Environment Simulation and Pollution Control, College of Environmental Sciences and Engineering, Peking University, Beijing 100871, China

[f] Department of unclear safety, Chia Institute of Atomic Energy, Beijing, 102413, China

[g] School of Earth and Space Sciences, University of Science and Technology of China, Hefei, 230026, China.

[h] School of Environmental Science and Optoelectronic Technology, University of Science and Technology of China, Hefei, 230026, China

[i] Shanghai Key Laboratory of Atmospheric Particle Pollution and Prevention (LAP^3), Department of Environmental Science and Engineering, Fudan University, Shanghai, 200433, China

*Corresponding authors: Cheng Liu (chliu81@ustc.edu.cn); Keding Lu (k.lu@pku.edu.cn)

ABSTRACT

Ship based multi-axis differential optical absorption spectroscopy (MAX-DOAS) measurements were ~~carried out~~conducted along the marginal seas of China from 19 April to 16 May 2018~~,~~ to measures the vertical profiles of aerosol, nitrogen dioxide (NO_2), and nitrous acid (HONO). Along the cruise route, we found f~~F~~ive hot spots ~~of~~ with enhanced tropospheric NO_2 VCDs ~~were found~~ in Yangtze River Delta, Taiwan straits, Guangzhou-Hong Kong-Macao Greater Bay areas, Zhanjiang Port, and Qingdao port ~~with averaged NO_2 VCDs of 1.07×10^{16}, 1.30×10^{16}, 7.27×10^{15}, 5.34×10^{15}, and 3.12×10^{15} molec. cm^{-2}, respectively~~. Enhanced HONO concentrations could usually be observed under high-level aerosol and NO_2 conditions, ~~HONO~~ whereas the reverse was not always the case. ~~performs similar spatial distribution characteristics as NO_2 with averaged HONO VCDs in above five hot spot areas of 1.01×10^{15}, 7.91×10^{14}, 6.02×10^{14}, 5.36×10^{14}, and 5.17×10^{14} molec. cm^{-2}, respectively. The averaged near surface NO_2 concentrations were 8.46 and 11.31 ppb, and the averaged near surface HONO concentrations were 0.23 and 0.27 ppb under sea oriented and land oriented observation azimuths during the whole campaign, respectively.~~ To understand the impacts of relative humidity (RH), temperature, and aerosol on the heterogeneous reaction of NO_2 to form HONO in different scenes, ~~The~~ the Chinese Academy of Meteorological Sciences (CAMS) and Southern University of Science and Technology (SUST) MAX-DOAS stations were selected as the inland and coastal cases, respectively ~~to further understand the impacts of relative humidity (RH), temperature, and solar radiation intensity (SRI) on the heterogeneous reaction of NO_2 to form HONO in different scenes~~. ~~The emission ratios of $\Delta HONO / \Delta NO_x$ in sea, CAMS and SUST were $0.46\pm0.31\%$, $0.82\pm0.34\%$, and $0.79\pm0.31\%$, respectively.~~ The RH turning points in CAMS and SUST cases were ~~all~~ both ~65% (60~~–~~70%), ~~however,~~whereas two turning peaks (~60% and ~85%) of RH were found in the sea cases. As temperature increased, t~~T~~he HONO/NO_2 ratio decreased ~~along with the increase of temperature, and~~ with peak values appearing ~~on~~ at ~12.5℃ in CAMS~~.~~, whereas t~~T~~he HONO/NO_2 gradually increased ~~along with increasing temperature,~~ and ~~with~~ reached peak values ~~on~~ at ~31.5℃ in SUST. In the sea case, when the temperature exceeded 18.0℃ ~~In sea case,~~, the HONO/NO_2 ratio ~~increase~~ rose ~~along~~ with ~~the~~ increase ~~of~~ing temperature ~~with~~ and achieved its peak~~a peak value~~ ~~on~~ at ~25.0℃, ~~under the temperature being larger than 18.0℃.~~ Th~~at~~is ~~means~~ indicated that ~~the~~ high temperature ~~could~~ can contribute to the secondary formation of HONO in the sea atmosphere. In the inland case, the correlation analysis between HONO and aerosol in the near-surface layer showed that the ground surface is more crucial to the formation of HONO via the heterogeneous reaction of NO_2; however, in

the coastal and sea cases, the aerosol surface contributed more. The correlation analysis between HONO and aerosol in near-surface layer illustrated the ground surface plays a more important role than aerosol surface during the HONO formation process from the heterogeneous reaction of NO_2 under inland case, however, aerosol surface plays a more important role during above process under coastal and sea cases. Moreover Furthermore, we found discovered that the conversion rate of HONO generation rate from NO_2 to HONO through heterogeneous reaction in the sea case is larger than that in the inland case in higher atmospheric layers (> 600 m) in higher atmospheric layers above 600 m. Three typical events were selected to demonstrate three potential contributing factors of HONO production under marine condition (i.e., transport, NO_2 heterogeneous reaction and unknown HONO source). This study elucidates the sea-land and vertical differences in the forming mechanism of HONO via the NO_2 heterogeneous reaction and provides deep insights into tropospheric HONO distribution, transforming process and environmental effects.

1 Introduction

Nitrous acid (HONO) is an important part of the atmospheric nitrogen cycle, and plays a significant role in atmospheric oxidation capacity (Alicke et al., 2003; Kleffmann et al., 2005). Photolysis of HONO in near ultraviolet bands (Eq. 1) is a substantial source of hydroxyl radicals (OH radicals), which are one of the most important oxidants in the tropospheric atmosphere. Previous Earlier studies reported that the contribution of HONO photolysis to OH radicals can reach 40–60%, and even more than while exceeding 80% especially in the early morning (Michoud et al., 2012; Ryan et al., 2018; Xue et al., 2020). OH radicals are one of the most important oxidants in the atmosphere. OH radicals They can oxidize and destroy most atmospheric pollutants, such as CO, NO_x ($NO+NO_2$), SO_2 and volatile organic compounds (VOCs), thereby further promoting the formation of secondary pollutants (e.g., ozone (O_3), peroxyacetyl nitrate (PAN), and secondary aerosols, etc.), and leading to serious haze pollution events (Huang et al., 2014). In addition Additionally, as a nitrosating agent, HONO can produce carcinogenic nitrite amines to that pose a threat to human health (Zhang et al., 2015). Therefore, a full understanding of the source and formation mechanism of HONO is has very important scientifically significance significant for the study of tropospheric oxidation and the control of secondary pollution.

At present Currently, the known sources of HONO mainly include direct emissions from vehicles, ships, biomass burning and soil, the homogeneous reaction of NO and OH radicals (Eq. 2), the nighttime and daytime heterogeneous reaction of NO_2 (Eq. 3) on aerosols, vegetation, ground and other types of surfaces, and the photolysis of nitrate particles (Eq. 4) (NO_3^-) (Alicke et al., 2003; Stemmer et al., 2006; Indarto et al., 2012; Wang et al., 2015; Salgado and Rossi, 2002; Zhou et al., 2011). There are also some obvious unknown Sources of HONO exist sources that are poorly understood (Fu et al., 2019). The heterogeneous reaction of NO_2 as a source of HONO has received continuous attention in recent years. It has been was found that the heterogeneous reaction of NO_2 is one of the most important sources of HONO in a variety of scenarios scenes such as inland, coastal cities and offshore seas. Liu et al. (2021) reported the contribution of heterogeneous reaction of NO_2 on aerosol surface to HONO is 19.2% in summer, and this contribution of heterogeneous reaction of NO_2 on aerosol and ground surfaces to HONO can reach 54.6% in winter in Beijing. Yang et al. (2021) and Zha et al. (2014) found that the generation rate of HONO through the heterogeneous reaction of NO_2 under sea-wind conditions could elevate 3-4 times than that under land-wind conditions in the northern coastal city of Qingdao and the southern coastal city of Hong Kong, respectively. Cui et al. (2019) illustrated that the heterogeneous reaction of NO_2 on aerosol and sea surfaces is an important source of HONO in East China Sea in summer. The process of HONO formed from the heterogeneous reaction of NO_2 is affected by various atmospheric parameters. The relative humidity (RH), temperature, solar radiation intensity (SRI), and aerosol concentration and its relative surface area are the particularly important parameters. Previous Earlier works always used the linear regression relationship between HONO/NO_2 and the above parameters to characterize the influence of these parameters on the formation of HONO through the heterogeneous reaction of NO_2. Although this kind of simple linear regression method may lead to artificial correlations and misleading conclusions, considering the vertical evolution of atmospheric parameters. Wen et al. (2019) found that the increased temperature could promote the heterogeneous reaction of NO_2 to form HONO in sea conditions. The generation rate of HONO could increase rapidly, when the temperature was greater than 20 ℃. Gil et al. (2019) found that the HONO formed from the heterogeneous reaction of NO_2 will increase along with the increase of RH when RH was less than 80% in a case of land park using deep learning forced by measurement results. Fu et al. (2019) reported that RH and SRI were the main parameters driving the heterogeneous reaction of NO_2 to form HONO in Pearl River Delta, and it contributes to 72% of the total source of HONO. Cui et al. (2019) found that the potential of heterogeneous reaction of NO_2 to form HONO will increase with the increase of particle concentration and the specific surface area of single particle in coastal cities.

$$HONO + h\nu \rightarrow NO + \cdot OH \ (\lambda < 400nm) \quad (1)$$

$$\cdot OH + NO + M \rightarrow HONO + M \quad (2)$$

$$2NO_2 + H_2O \rightarrow HONO + HNO_3 \quad (3)$$

$$HNO_3 / NO_3^- + h\nu \rightarrow HONO / NO_2^- + O \cdot (\lambda \sim 300nm) \quad (4)$$

However, ~~previous~~ earlier researches generally focus~~es~~ on the near-surface layer of a single scene, and attentions ~~on~~ to the influence mechanism of the heterogeneous reaction of NO_2 to form HONO in vertical direction and in different sea and land scenes are insufficient, which limits the comprehensive assessment to understand the sea-land differences and impact mechanism of HONO formed from the heterogeneous reaction of NO_2. NO_2 could be transported from inland and coastal cities to offshore seas (Tan et al., 2018). This part of NO_2 can promote the HONO formation through heterogeneous reaction on the high-level aerosol and sea surfaces in the atmosphere of sea (Zhang et al., 2020). The formed HONO is ~~completely~~ likely to be ~~transported~~ carried to land cities at night by sea breeze~~under favorable weather conditions~~. ~~It~~ which will affect the atmospheric oxidation and air quality, and even endanger human health. ~~In a~~Additionally, the vertical distributions and values of atmospheric meteorology and aerosol parameters are significantly different in land and sea scenes, which provide different conditions for the heterogeneous reaction of NO_2 to form HONO in different height layers. ~~Moreover~~Furthermore, aerosols and NO_2 have complex evolution and transmission characteristics in the vertical direction. The vertical upward transport of aerosol and NO_2 can promote the HONO formation through heterogeneous reaction at high altitude, and the vertical downward transport of HONO will impact the atmospheric environment near the ground. The vertical observations in land-sea scenes ~~is~~ are also helpful to distinguish the contribution of the heterogeneous reaction of NO_2 on the aerosol and ground/sea surfaces (Zhang et al., 2020).

~~At present~~Currently, a variety of HONO measurement techniques have been developed, which in principle can be roughly divided into wet chemical ~~methods~~, spectroscopy ~~methods~~, and mass spectrometry methods~~, in principle~~ (Cheng et al., 2013; Bernard et al., 2016; Gil et al., 2019; Guo et al., 2020; Jordan et al., 2020). However, these technical methods can only measure the HONO information near the surface layer. Taking tower and aircraft as platforms, these techniques were performed to measure HONO vertical profiles, and it was found that the peak values of HONO usually appeared under 200 m at urban and suburban areas (Kleffmann et al., 2003; Stemmler et al., 2006; Zhang et al., 2009; Wong et al., 2012; Meng et al., 2020; Zhang et al., 2020). These studies also revealed that the heterogeneous reaction of NO_2 on multiple surfaces (ground and aerosol etc.) was an important source of HONO under planetary boundary layer (PBL), especially in haze days. ~~Moreover~~Furthermore, they also reported that the HONO/NO_2 ratios usually decreased with the increase of height under 200 m at inland and coastal areas. ~~Zhang et al. (2020) measured the vertical distribution of HONO by placing wet chemical HONO samplers at different heights of tower in Being during spring, and found the maximum value of HONO appeared at 120 m sourced from the heterogeneous reaction of NO_2 on aerosol surface under haze conditions. Meng et al. (2020) also used tower by moving the IBBCEAS carried in a box at a constant speed to measure the vertical profiles of HONO in Beijing during winter, and reported that the heterogeneous reaction of NO_2 under the atmospheric boundary layer is an important source of HONO, especially in haze conditions.~~ However, the cost of above techniques used to measure HONO vertical profiles was too high, and the real-time and continuous measurement cannot be realized. Multi-axis differential optical absorption spectroscopy (MAX-DOAS), as a ground-based ultra-hyperspectral remote sensing technology, ~~had been~~was widely used for vertical observation of atmospheric pollutants in the past two decades. ~~Therefore, the measurement of the vertical profiles of HONO under different sea-land scenes based on MAX-DOAS could provide technical supports for learning the sea-land and vertical differences and the influence mechanism of the heterogeneous reaction of NO_2 to form HONO.~~ In the past five years, several researchers ~~have~~ carried out campaigns based on MAX-DOAS to measure the vertical profile of HONO in inland and coastal areas, and revealed their vertical characteristics, sources and the contribution to ~~the sources of HONO and their contribution to~~ atmospheric oxidation at different height layers (Garcia-Nieto et al., 2018; Ryan et al., 2018; Wang et al., 2020; Xing et al., 2021; Xu et al., 2021; He et al., 2023). ~~There were f~~Few studies were conducted on the sources of HONO at different height layers in sea conditions. In this study, ~~it will be the first time to use~~ MAX-DOAS is used for the first time to study the spatiotemporal distribution and the sources of HONO along the Chinese coastline, and to learn the differences of the HONO formed from the heterogeneous reaction of NO_2 in different height layers and land-sea scenes.

2 Methods and methodologies

2.1 ~~The m~~Measurement cruise

The ship-based atmospheric observation campaign along the marginal seas of China was ~~carried out~~conducted from 19 April to 16 May 2018. The latitude and longitude ranges of the entire campaign covered 21.12°N–35.89°N and 110.67°E–122.16°E. The detailed voyage records of the observation ship are shown in Table 1. An integrated and fully automated MAX-DOAS instrument was installed aboard the stern deck of the ship (Figure S1(a)). ~~In order t~~To ensure that the instrument is always kept in a horizontal position, a photoelectric gyro was used. The angle between the observation ~~direction~~ and ~~the~~ heading direction~~s~~ of the ship was always maintained at 135° during the whole campaign. The telescope unit of the instrument pointed towards sea during cruise NO.3 and NO.6. The telescope unit pointed towards inland during cruise NO.1, NO.4 and NO.5. During cruise NO.2, the observation telescope always pointed to Chongming island. The measurement ship only sailed in daytime from 19 April to 02 May, and

continuously sailed in all the daytime and nighttime from 3 May to 16 May 2018. The ship docked in Daishan port on 9–10 May and no observations were ~~carried out~~conducted during these two days.

The aim of this campaign was to learn the vertical differences of NO_2 heterogeneous reaction to produce HONO in marginal seas of China and compare the influence mechanism of that in inland cities. ~~In order t~~To fully understand the differences of the impacts of RH, temperature and aerosol on the HONO secondary formation in land and sea conditions, the Chinese Academy of Meteorological Sciences (CAMS) and Southern University of Science and Technology (SUST) MAX-DOAS stations were selected as inland and coastal areas for analysis, respectively. CAMS ~~was~~ is located in the urban of Beijing (116.32°E, 39.94°N), and SUST ~~was~~ is located in Shenzhen (114.00°E, 22.60°N) (Figure S2). This study will provide scientific guidance for understanding regional oxidation capacity and controlling the secondary air pollution.

2.2 MAX-DOAS measurements

2.2.1 Instrument setup

The compact instrument consists of an ultraviolet spectrometer (AvaSpec-ULS2048L-USB2, 300-460 nm spectral range, 0.6 nm spectral resolution) at a 20℃ fixed temperature with a deviation of < 0.01℃, a one-dimensional CCD detector (Sony ILX511, 2048 individual pixels) and a telescope unit driven by a stepper motor to collect scattered sunlight from different elevation angles. The accuracy of elevation angle is < 0.1 ℃and the telescope field of view (open angle) is < 0.3°. A full scanning sequence consists of 11 elevation angles (1°, 2°, 3°, 4°, 5°, 6°, 8°, 10°, 15°, 30° and 90°). The integration time of one individual spectrum was set to 30 s, and each scanning sequence took about 5.5 min. Besides, the controlling electronic devices and connecting fiber are mounted inside. The instrument is equipped with a high-precision Global Position System (GPS) to record the real-time coordinated positions of the ~~ship~~ cruise ship. The detailed description of the setup of MAX-DOAS in CAMS and SUST can be found in Liu et al. (2021).

2.2.2 Data processing and filtering

The MAX-DOAS measurements could be influenced by the exhaust from the measurement ship. Therefore, the data contaminated by the exhaust were filtered out. As shown in Figure S1(b), the direction and speed of the plume exhausted from the ship depends on the ship ~~direction/speed~~ and the true wind speeds/directions. Individual measurements taken under unfavorable plume directions (plume directions between 45 and 135◦ with respect to the heading of the ship) were discarded. ~~In order t~~To avoid the strong influence of the stratospheric absorption, the spectra measured with solar zenith angle (SZA) lager than 75° were filtered out. Under these two filtering criteria, 4.9 and 8.3% of all data were rejected before DOAS analysis (Xing et al., 2017, 2019, 2020).

2.2.3 DOAS analysis

The MAX-DOAS measured spectra were analyzed using the software QDOAS which is developed by BIRA-IASB (http://uv-vis aeronomie.be/software/QDOAS/). The DOAS fit results are the differential slant column densities (DSCDs), i.e. the difference of the slant column density (SCD) between the off-zenith ~~spectrum~~ and the corresponding zenith reference ~~spectrum~~spectra. Details of the DOAS fit settings are listed in Table1. A typical DOAS retrieval example for the oxygen dimer (O_4), nitrogen dioxide (NO_2) and nitrous acid (HONO) are shown in Figure 1. The stratospheric contribution was approximately eliminated by taking the zenith spectra of each scan as reference in the DOAS analysis. Before profile retrieval, DOAS fit results of O_4, NO_2 and HONO with root mean square (RMS) of residuals larger than 3×10^{-3} were filtered. ~~Moreover~~Furthermore, the SCD data under the color index (CI) being < 10% of the thresholds obtained through fitting a fifth-order polynomial to CI data which is a function of time was filtered out, ~~in order~~ to ensure a high signal-to-noise ratio (SNR) of the spectra. This filtering criteria remove 2.1, 3.9, and 5.3% for O_4, NO_2 and HONO, respectively.

2.3 Vertical profile retrieval

Aerosol and trace gases (i.e., NO_2 and HONO) vertical profiles are retrieved from MAX-DOAS measurements using the algorithm reported by Liu et al. (2021). The inversion algorithm is developed based on the Optical Estimation Method (OEM) (Rodgers, 2000), which employs the radiative transfer model VLIDORT as the forward model. The detailed retrieval procedure is displayed in Appendix I and Figure S3.

In this study, an exponential decreasing a priori with a scale height of 1.0 km was used as the initial profile for both the aerosol and trace gases retrieval (Figure S4). The surface concentrations of aerosol ~~and trace gases, NO_2, and~~ HONO were set to 0.~~3~~2 km^{-1}, 3.0 ppb, and ~~5~~1.0 ppb, respectively. We assume a fix set of aerosol optical properties with asymmetry parameter of 0.69, a single scattering albedo of 0.90 and ground albedo of 0.05. ~~Moreover~~Furthermore, the uncertainty of the aerosol and trace gases a priori profile was set to 100% and the correlation length was set to 0.5 km. The averaging kernels indicated that the sensitivity of the profile retrieval tended to decrease with increasing altitude, and was especially sensitive to the layers within 0–1.5 km (Figure S5). The sum of the diagonal elements in the averaging kernel matrix is the degrees of freedom (DOF), which denotes the number of independent pieces of information contained in the measurements.

2.4 Error analysis

For profile retrieval, the error sources can be divided into four different types: smoothing error, measurement noise error, forward model error, and model parameter error (Rodgers, 2004). However, in terms of this classification, some errors are difficult to be calculated or estimated. For example, forward model error, which is caused by an imperfect representation of the physics of the system, is hard to be quantified due to the difficulty of acquiring an improved forward model. Given calculation convenience and contributing ratios of different errors in total error budget, we mainly took into account error sources based on the following classification, which were smoothing and noise error, algorithm error, cross section error and uncertainty related to the aerosol retrieval (only for trace gas). Here, we estimated the contribution of different error sources to the trace gas vertical column densities (VCDs) and AOD, and near-surface (0–200 m) trace gas concentrations and aerosol extinction coefficients (AECs), respectively. The detailed demonstrations and estimation methods are displayed below, and the final results are summarized in Table 3.

a. Smoothing errors arise from the limited vertical resolution of profile retrieval. Measurement noise errors denote the noise in the spectra (i.e., the fitting error of DOAS fits). They can be quantified by averaging the error of retrieved profiles, as the error of the retrieved state vector equals the sum of these two independent errors. We calculated the sum of smoothing and noise errors on near-surface concentrations and column densities, which were 14 and 5 % for aerosols, 16 and 17 % for NO_2, and 20 and 22 % for HONO, respectively in the sea scene. The corresponding values were 13 and 5 % for aerosols, 14 and 16 % for NO_2, and 18 and 20 % for HONO, respectively at SUST and 13 and 5 % for aerosols, 15 and 17 % for NO_2, and 19 and 21 % for HONO at CAMS.

b. Algorithm error is the discrepancy between the measured $\boldsymbol{y}$ and modelled DSCDs $\boldsymbol{F(x,b)}$. This error contains forward model error from an imperfect approximation of forward function (e.g., spatial inhomogeneities of absorbers and aerosols), forward model parameter error from selection of parameters $\boldsymbol{b}$, and error not related to the forward function parameters, such as detector noise (Rodgers, 2004). Algorithm error is a function of the viewing angle, and it is difficult to assign this error to each altitude of profile. Usually, the algorithm errors on the near-surface values and column densities are estimated by calculating the average relative differences between the measured and modeled DSCDs at the minimum and maximum elevation angle (except 90 °), respectively (Wagner et al., 2004). Considering its trivial role in the total error budget, we estimated these errors on the near-surface values and the column densities at 4 and 8 % for aerosols, 3 and 11 % for NO_2, and 20 and 20 % for HONO, according to Wang et al. (2017) and Wang et al. (2020).

c. Cross section error is the error arising from an uncertainty in the cross section. According to Thalman and Volkamer, (2013), Vandaele et al. (1998), and Stutz et al. (2000), we adopted 4, 3, and 5 % for O_4 (aerosols), NO_2, and HONO, respectively.

d. The trace gas profile retrieval error represents the one, which is sourced from aerosol extinction profile retrieval and propagated to retrieved trace gas profile. This error could be roughly estimated based on a linear propagation of the total error budgets of the aerosol retrievals. The errors of trace gases were roughly estimated at 15% for VCDs and 10% for near-surface concentrations for the two trace gases in the sea scene. The corresponding values were 14 and 10 % for near-surface concentrations and VCDs, respectively at SUST, and 14 and 10 % at CAMS.

The total uncertainty was calculated by adding all the error terms in the Gaussian error propagation, and the final results were listed in the bottom row of Table 3. We found that the sum of smoothing and noise errors played a dominant role in the total uncertainty.

2.54 Ancillary data

Meteorological data (including temperature, pressure, relative humidity, visibility, solar radiation intensity, wind speed and wind direction) with a temporal resolution of 1 min was measured in the weather station installed on the ship. NO was measured using NO analyzer (Thermo Scientific model 42i) with a 1 min ~~time~~ resolution. The speed of the ship was calculated referred to the GPS data.

The temperature and relative humidity of two ground-based stations (i.e., CAMS and SUST) were collected from Weather Underground website, temporal resolution of which is around 3 hours.

The backward trajectory was calculated using HYSPLIT (Hybrid Single-Particle Lagrangian Integrated Trajectory) developed by the National Oceanic and Atmospheric Administration Air Resource Laboratory (NOAA-ARL). The meteorological data with a 1°×1° spatial resolution and 24 layers were collected from the Global Data Assimilation System (GDAS).

3 Results and Discussion

3.1 Overview of the MAX-DOAS observation over marginal seas of China

A radiative transfer model SCIATRAN was used to convert SCDs of NO_2 and HONO to their tropospheric ~~vertical column densities (~~VCDs~~)~~. The vertical profiles of aerosol, NO_2 and HONO retrieved from MAX-DOAS, the temperature and pressure vertical profiles simulated using a dynamical-chemical model (WRF-Chem), and the geo-position data collected by GPS were introduced as inputs in SCIATRAN for the NO_2 and HONO air mass factor (AMF) calculation. Missing data are due to power and instrument system failure, interference of ship plume, unfavorable weather condition (i. e., heavy rain), and night sailing. During the cruise of Chongming to Zhanjiang, NO_2 VCDs varied from 1.05×10^{14} to 4.02×10^{16} molec.cm^{-2} with an averaged value of 3.90×10^{15} molec. cm^{-2}. From

Zhanjiang to Qingdao, NO_2 VCDs varied from 1.08×10^{14} to 2.60×10^{16} molec.cm^{-2} with an averaged value of 4.27×10^{15} molec. cm^{-2} ~~from Zhanjiang to Qingdao~~. From Chongming to Zhanjiang, HONO VCDs varied from 1.00×10^{14} to 2.58×10^{15} molec. cm^{-2} with a mean value of 2.39×10^{14}molec. cm^{-2}. From Zhanjiang to Qingdao, HONO VCDs varied from 1.01×10^{14} to 2.61×10^{15}molec. cm^{-2} with a mean value of 2.74×10^{14} molec. cm^{-2}.

Figure 2 showed the spatial distribution of NO_2 and HONO VCDs over the marginal seas of China. ~~It should be noted that f~~Five ~~elevated~~ enhanced tropospheric NO_2 VCDs hot spots were observed during the whole campaign, i.e., the coastal areas of Yangtze River Delta, Taiwan straits, Guangzhou-Hong Kong-Macao Greater Bay areas, Zhanjiang Port, and Qingdao port. In the coastal areas of Yangtze River Delta, the hot spots were mainly distributed in the Yangtze River estuary, Hangzhou Bay, Ningbo port, Taizhou port, and Wenzhou port. These areas are mostly important shipping channels or shipping ports, and are great NO_2 emission sources. The averaged NO_2 VCDs in above five areas reached 1.07×10^{16}, 1.30×10^{16}, 7.27×10^{15}, 5.34×10^{15}, and 3.12×10^{15} molec. cm^{-2}, respectively (Figure S6(a)). HONO exhibited similar spatial distribution characteristics as NO_2, and the averaged HONO VCDs in above five hot-spot areas reached 1.01×10^{15}, 7.91×10^{14}, 6.02×10^{14}, 5.36×10^{14}, and 5.17×10^{14} molec. cm^{-2}, respectively (Figure S6(b)). It indicates that NO_2 is an important precursor of HONO. ~~Previous~~ Earlier studies ~~have~~ reported that HONO can ~~be produced~~ generated from NO_2 through heterogeneous reaction on the surface of aerosol and sea (Yang et al., 2021). However, there are obvious differences in the concentration distribution of HONO and NO_2 in the southeast coastal area of Jiangsu (from Qidong to Dongtai). In this area, NO_2 showed a higher concentration (1.66×10^{16} molec. cm^{-2}, which is 4 times higher than the mean NO_2 VCD), while HONO showed a lower concentration (2.06×10^{14} molec. cm^{-2}, which is ~80% of the mean HONO VCD). It ~~migh~~may~~t~~ be the fresh ship emission plume on the route enhancing the NO_2 concentration and HONO has not been fully formed from NO_2 heterogeneous reaction in time, ~~due to~~since the observations from ship-based MAX-DOAS are instantaneous. ~~On the other hand, the solar radiation intensity in this day (12 May, 2018) was significantly lower than other days (Fig. S2), and this weather condition was not conductive to the HONO formation through the heterogeneous reaction of NO_2.~~

The surface concentration of NO_2 and HONO were extracted from their corresponding vertical profiles. As shown in Figure 3, the total averaged near-surface NO_2 concentrations under sea-oriented and land-oriented measurements were 8.46 and 11.31 ppb, respectively. The total averaged near-surface HONO concentrations were 0.23 and 0.27 ppb under sea-oriented and land-oriented measurements. The total averaged near-surface HONO/NO_2 ratios in sea-oriented and land-oriented measurements were 0.027 and 0.024, respectively. ~~Previous~~ Earlier studies reported that vehicle and ship emissions were the main primary HONO sources on land and sea, respectively, and NO_2 heterogeneous reaction on the surfaces of ground, sea, vegetation and aerosol were the ~~HONO~~ important secondary HONO sources (Liu et al., 2021). Additionally, t~~T~~hey also found that the surface HONO concentration under the sea case was lower than that under the land case, especially in the morning and evening (Yang et al., 2021). Figure 4 showed the time series of AOD, the surface concentrations of NO_2 and HONO, and the surface HONO/NO_2 during the whole campaign. We ~~could find~~found that the time series of AOD and NO_2 were similar. The high AOD and NO_2 usually appeared in busy shipping channels and ports, and the obvious high-value areas were the coast of the Yangtze River Delta, the Taiwan Strait, Xiamen port, Zhanjiang port and Qingdao port (with mean AOD and NO_2 of 1.28 and ~~mean NO_2 of~~ 18.90 ppb, respectively). HONO always appeared under high AOD and NO_2 conditions, however, high AOD and NO_2 were not necessarily accompanied with high ~~production rate of~~ HONO concentration. This was because the heterogeneous formation of HONO requires suitable meteorological conditions (i.e., RH and temperature) in addition to its precursor (NO_2) and the reaction surface (aerosol) (Liu et al., 2019). The high HONO/NO_2 values were found on 02, 13 and 14 May with an average value of 0.45 ~~during the whole campaign~~. ~~Moreover~~Furthermore, we found the high values of HONO/NO_2 always appeared from 11:00 to 14:00 during a whole day. ~~That is due to the high production rate of HONO and the high photolysis rate of NO_2 during noontime.~~

3.2 ~~The r~~Relationship between HONO/NO_2 with RH, Temperature, and aerosol in land and sea

~~In order to fully understand the differences of the impacts of RH, temperature and aerosol on the HONO secondary formation in land and sea conditions, the Chinese Academy of Meteorological Sciences (CAMS) and Southern University of Science and Technology (SUST) MAX-DOAS stations were selected as inland and coastal areas for analysis, respectively.~~ Sun et al. (2020) reported that HONO concentrations could increase up to 40–100% over the shipping routes and international ports~~navigation areas~~, and Huang et al. (2017) reported vehicle exhaust could contribute to ~12–49% of the atmospheric HONO budget. Since the direct emissions of the measurement ship ~~have been~~were removed before data analysis, the primary source of HONO during the whole campaign was mainly from the direct emissions of cargo ships. By subtracting the average marine background of NO_x and HONO from the ship plume emission values, the impact of background values is reduced and the emission ratio of $\Delta HONO / \Delta NO_x$ can be obtained, and this emission ratio can be used for quantifying the primary HONO (Sun et al., 2020; Xu et al., 2015). In this study, w~~W~~e used an averaged $0.46\pm0.31\%$ emission ratio of $\Delta HONO / \Delta NO_x$ ~~in this study~~ referring to Sun et al. (2020) to understand the primary source of HONO on the sea surface during the campaign. The NO was measured using in situ instrument, and sea-surface NO_2 was extracted from the retrieved NO_2 vertical profiles (NO_x = NO + NO_2). ~~In a~~Additionally, the calculation method of emission ratios of $\Delta HONO / \Delta NO_x$ in CAMS and SUST was

referred ~~to~~ from Xu et al. (2015), Liu et al. (2018), and Xing et al. (2021) (Appendix II). The averaged emission ratios in CAMS and SUST were 0.82±0.34% and 0.79±0.31%, respectively. The direct emissions ~~have been~~were deduced in the following study of the secondary formation of HONO. The ratios of HONO/NO_2 in CAMS, SUST and the ship-based campaign could be found in Figure ~~S3~~S7. ~~Moreover~~Furthermore, the main secondary formation pathway of HONO ~~are~~ is ~~believed mainly from~~considered as the heterogeneous reaction of NO_2 on the surface. The linear regression between HONO and NO_2 in land and static sea scenarios is shown in Figure 5. We found the fitting slopes in static sea scenes was ~8–10 times larger than that in land scenes, especially on sea-oriented measurements under static weather condition (slope ≈ 0.06). The correlation coefficients (R) in inland and static sea ~~scenes~~ scenarios were all > 0.62, except in SUST (R = 0.58). ~~That~~, which indicates the formation rate of secondary HONO from NO_2 heterogeneous reaction in static sea ~~scenes~~ scenarios ~~might~~ may be faster than that in land ~~scenes~~scenarios. The corresponding temperature and RH conditions of each spot are displayed in Figure S8, which roughly reveals the impact of RH and temperature on the process of NO_2 forming HONO through heterogeneous reactions.

3.2.1 RH dependence on HONO formation

The scatter plots of HONO/NO_2 against RH in different land and sea conditions are illustrated in Figure 6. The highest values can represent varying range of data in each interval and reveal concentration levels of data distribution. ~~In order t~~To eliminate the influence of other factors, the average of the six highest HONO/NO_2 in each 10% RH interval is calculated to reflect the distribution range of data in each interval (Liu et al., 2019). The dependence of the averaged top-6 HONO/NO_2 on RH reveal an overall variation tendency of HONO/NO_2 against RH. ~~We found the RH turning points i~~In the inland (CAMS) and coastal (SUST) cases, the RH turning points are ~~all~~ both ~65% (60–70%), where increasing trend switches to decreasing tendency. The HONO/NO_2 increases along with RH when RH is less than 65%, and the HONO/NO_2 will decrease when RH is larger than 65%. ~~That means~~which implies that it contributes to the HONO formation from the heterogeneous reaction of NO_2 on wet surfaces with the gradual increase of RH until 65%. The decrease of HONO/NO_2 with RH larger than 65% is presumably due to the efficient uptake of HONO on wet surfaces and the wet surfaces being less accessible or less reactive to NO_2 when RH being larger than 65% (Liu et al., 2019). However, two turning peaks of RH were found in the sea cases. The first RH turning peak occurred in ~60%, which is the similar ~~with~~ to that under the inland and coastal cases. ~~While~~ and another RH turning peak appeared in ~85% (80–90%). ~~That~~ This ~~mean~~implies that high RH also could increase the HONO formation in sea cases. ~~A~~In addition, the HONO/NO_2 decreased sharply when RH was larger than 95%, because the reaction surface will asymptotically approach a water droplet state to limit the formation of HONO with RH larger than 95%.

3.2.2 Temperature dependence on HONO formation

The scatter plots of HONO/NO_2 against temperature in different land and sea conditions are shown in Figure 7. Similar to the scatter plots of HONO/NO_2 against RH, we also adopted ~~To eliminate the influence of other factors,~~ the averaged ~~of the six highest~~top-6 HONO/NO_2 values in each 5℃ ~~temperature~~ interval ~~is calculated~~to represent a general variation tendency of HONO/NO_2 against temperature. In the inland condition (CAMS), the HONO/NO_2 decreased along with the increase of temperature, and the highest values of HONO/NO_2 ~~peak values~~ appeared ~~on~~ at ~~the temperature being~~ ~12.5℃. However, we found ~~the~~ that HONO/NO_2 increased along with the increase in temperature, and the highest values of HONO/NO_2 appeared ~~with~~ at ~31.5℃ ~~temperature~~ in coastal condition (SUST). ~~That~~ which indicates that the HONO formation from NO_2 heterogeneous reaction will be accelerated under lower and higher temperature in the inland and coastal conditions, respectively. In the sea condition, the HONO/NO_2 increased along with the increase ~~of~~ in temperature with a high value under ~25.0℃ ~~temperature~~ when the atmospheric temperature was larger than 18.0℃, and simultaneously, a ~1.9 averaged HONO/NO_2 high value was found under ~15.0℃ (14.0–17.0℃) ~~temperature~~. ~~Moreover~~Furthermore, we found that the appearance of HONO/NO_2 high values under lower temperature (14.0–17.0℃) was usually accompanied by ~~landing wind~~land breeze. Wen et al. (2019) also reported that relatively high temperature could contribute to the formation of HONO in the sea condition.

3.2.3 Impact of aerosol on HONO formation

~~In order t~~To further understand the HONO formation from NO_2 heterogeneous reaction on aerosol surface, several correlation analyses were ~~carried out~~conducted. As shown in Figure 8, the linear regression plot~~s~~ between HONO and aerosol~~, and between HONO/NO_2 and aerosol~~ in land and sea conditions ~~were~~ was performed. It was found that the correlation coefficient (R) between HONO and aerosol varied in the order of coastal (0.55) > sea (0.51) > inland (0.14). ~~In a~~Additionally, the fitting slopes under coastal and sea conditions (0.07) are about 2.3 times larger than that under inland condition (0.03). ~~That means~~which implies that the ground surface maybe more important than aerosol surface during the process of HONO formed from NO_2 heterogeneous reaction in the ground surface layer of the inland. In the coastal and sea conditions, the aerosol and sea are ~~all~~ both important ~~to~~ in providinge heterogeneous reaction surface for NO_2 to form HONO (Cui et al., 2019; Wen et al., 2019; Yang et al., 2021). ~~In a~~Additionally, we found the averaged values of HONO/NO_2 were 0.011±0.004, 0.014±0.006, 0.008±0.003 and 0.007±0.003~~are 0.011, 0.014 and 0.008~~ when aerosol extinctions are 0–0.3, 0.3–0.6, ~~and~~ 0.6–0.9 and > 0.9 km^{-1} in the inland case,

respectively (Figure 8(b)). As shown in Figure 8, tThe high values of $HONO/NO_2$ are were mainly under aerosol extinction being less than 1.0 km^{-1} with averaged values of 0.012 ±0.006 and 0.090 ±0.0040.16 and 0.32 in the coastal and sea cases, respectively. It indicates that aerosol surface plays a more important role to in forming HONO through NO_2 heterogeneous reaction in the sea condition than that in the land condition.

3.3 Vertical distributions of $HONO/NO_2$ under different aerosol condition in land and sea

In order tTo further investigate the height dependence of $HONO/NO_2$ under land and sea conditions, two cases in Pearl River Delta (PRD) were selected from the whole campaign. As shown in Figure 9, "A" and "B" were under similar aerosol level (the extinction coefficients in surface layer being 0.45-0.60 km^{-1}) and vertical distribution structure, and were all observed from 10:00 to 11:00. The instrument viewed sea accompanied with sea wind in "A" named sea scene, and the instrument viewed land accompanied with land wind in "B" named land scene. The NO_2 in the sea and land scenes have a similar vertical structure, and the NO_2 concentration in land scene are larger than that in sea scene except on the surface layer. The HONO have the same vertical distribution structure in the above two scenes, and the HONO concentration in the land scene always larger than that in the sea scene. In Figure 9(e), we found that $HONO/NO_2$ under 0 – 400 m in the land scene is higher than that in the sea scene, however, the $HONO/NO_2$ values are obviously lower in the land scene than that in the sea scene above 400 m. MoreoverFurthermore, the growth rate of $HONO/NO_2$ with the increase of height in the sea scene is significantly faster than that in the land scene above 400 m. It This indicates the generation rates of HONO sourced from NO_2 heterogeneous reaction on aerosol surface in the sea scene is larger than that in the land scene above 400 m. Under 400 m, the HONO generation rates in land scene is larger than that in the sea scene.

In aAdditionally, we selected inland cases (CAMS) to learn the difference of height dependence of $HONO/NO_2$ compared with sea scenes under different aerosol loads. As shown in Figure 10, the sea and inland scenes had the similar aerosol levels (low aerosol level: < 0.2 km^{-1}) and vertical structure. MoreoverFurthermore, the NO_2 and HONO in the sea and inland scenes have the similar vertical structure, but although their concentrations in the sea scene are all larger than that in the inland scene. In Figure 10(d), we could findfound that the $HONO/NO_2$ in the sea scene was obviously larger than that in the inland scene above 400 m. The $HONO/NO_2$ in the sea scene was about 4.5 times larger than that in the inland scene especially above 600 m. As shown in Figure 11, the aerosols under the sea and inland scenes were also with theexhibited similar extinction levels (relatively high level: ~0.8 km^{-1}) and vertical structure. The NO_2 concentration in the sea scene was higher than that in the inland scene but with a similar vertical structure. The HONO concentration in the sea scene was lower than that in the inland scene under 400 m, while it the concentration in the sea scene is was larger than that in the inland scene above 400 m. In Figure 11 (d), we found the $HONO/NO_2$ in the inland scene was larger than that in the sea scene under 600 m, while the $HONO/NO_2$ in the sea scene was about 2 times larger than that in the inland scene above 600 m. Above aAll the above cases indicated that the HONO generation rate from NO_2 heterogeneous reaction in the sea scene was larger than that in the inland scene in higher atmospheric layers above 400 – 600 m. The high-altitude (> 400 – 600 m) atmospheric parameters in the sea scene were more conductive to promote the HONO formation through the heterogeneous reaction of NO_2. As shown in Figure S4S9, the ratio of $HONO/NO_2$ also generally increased with the increase of in height above 0.2 km during the whole ship-based campaign. The greatest sensitivity under 1.5 km and the high degree of freedom (DOF) for aerosol, NO_2 and HONO gave confidence in the retrieval results (Figure S5S10).

3.4 Case study

The important factors and precursors to drive the formation of HONO through heterogeneous reaction had complex evolution and transport characteristics. To further clarify the role of these parameters in the heterogeneous process of NO_2 to form HONO, three typical processes were selected to reveal the favorable conditions for HONO formation at the sea scene.

3.4.1 20 April: A typical transport event

As shown in Figure 12, the aerosol mainly distributed in 0-200 m with a mean extinction coefficient larger than 0.74 km^{-1}. NO_2 was mainly distributed near the ground surface with a mean concentration of 28.54 ppb before 13:20. The NO_2 during this period might may come from local ship emissions, due toas this area is a main shipping channels. From 14:25 to 17:10, a high-concentration NO_2 air mass (averaged 13.29 ppb) was found at ~2.0 km. In order tTo understand thei source of this high-altitude NO_2 air mass, we further investigated the possible influence of transport by using the backward trajectories. We calculated 24 h backward trajectories of air masses at 500, 1000, and 2000 m using HYSPLIT (Figure S11) (Hybrid Single-Particle Lagrangian Integrated Trajectory) developed by the National Oceanic and Atmospheric Administration Air Resource Laboratory (NOAA-ARL). The meteorological data with a 1° ×1° spatial resolution and 24 layers were collected from the Global Data Assimilation System (GDAS). In Figure 13S11, we found that the dominant wind direction during this period was southeast at all heights, i.e., 500, 1000 and 2000 m. The transport of air masses carried NO_2 emitted by ships in Ningbo and Zhoushan ports, to main cargo ports of China and , to Shanghai. MoreoverFurthermore, the concentration of NO_2 was low (averaged 2.32 ppb) near the ground surface from 14:25 to 17:10. As shown in Figure 12 (e) and (g), a low pressure (< 1020 hPa), north dominant

wind direction with the wind speed > 12 m/s appeared at the ground surface during this period~~. That means, which~~ implies that the clean air from north reduced the local surface NO_2. The HONO was mainly distributed near the surface with a mean concentration of 0.07 ppb, and the two peaks were found ~~at~~ in the early morning (averaged 0.15 ppb) and at 12:15 (averaged 0.11 ppb), respectively (Figure ~~S6~~S12). The relatively high concentration of HONO ~~appeared~~ appearing in the early morning was possibly attributed to the ~~-~~accumulation~~ed~~ with the stabilization of boundary layer and attenuation of solar radiation after the sunset the day before (Xing et al., 2021). The HONO peak ~~appeared~~ appearing at 12:15 ~~might~~ may be sourced from the heterogeneous reaction of NO_2 on the aerosol surface under a ~80% RH, ~~a~~ 18.5℃ temperature, and ~~a~~ 1×10^3 W/m^2 SRI conditions.

3.4.2 28 April: A typical event of HONO produced from NO_2 heterogeneous reaction

From a typical port observation case, t~~T~~he measurement ship moored at Xiamen port on 28 April~~. This is a typical port observation case~~. As shown in Figure ~~14~~13, we found ~~there are~~ two peaks for aerosol and NO_2 ~~at~~ from 09:00~~-~~11:00 and 14:00~~-~~16:00 (averaged aerosol extinction coefficient > 0.8 km^{-1}, averaged NO_2 concentration > 12.0 ppb), respectively. NO_2 was mainly distributed near the sea surface layer 0~~-~~200 m, and ~~there was~~ a high-concentration NO_2 air mass ~~being~~ was found in 1.0~~-~~2.0 km during 13:00~~-~~14:00 due to the short distance transport of NO_2 emitted from ships in Xiamen port (Figure S13). However, aerosol appeared in the range of 0.0~~-~~2.0 km during 09:00~~-~~11:00 and 14:00~~-~~16:00. In Figure ~~14~~13 (g), we found that the wind speeds in the above two peak periods were obviously higher than that in other periods. ~~In~~ From 09:00~~-~~11:00, the wind speed was ~5.0 m/s with a northwest dominant direction (urban), and the wind speed was ~6.0 m/s with a southeast dominant direction (port gateway) during 14:00~~-~~16:00~~. That~~, which indicates that the short-distance high-altitude transport caused the appearance of high-extinction aerosol mass during the above two periods.

~~Moreover~~Furthermore, we found the high-concentration HONO only appeared at 14:00~~-~~16:00 with a 0.57 ppb averaged concentration under 0.9 km, while it was only about 0.14 ppb during 09:00~~-~~11:00 period. The slightly increase of RH and temperature (Tem) at 14:00~~-~~16:00 (RH: ~75.0%, Tem: 23.7℃) may contribute to HONO formation through heterogeneous reaction of NO_2 on the aerosol surface than that at 09:00-11:00 ~~The higher RH and temperature (Tem) (RH: ~75.0%, Tem: 23.7℃) at 14:00-16:00 than that (RH: ~67.6%, Tem: 23.1℃) at 09:00-11:00~~ (Figure ~~14~~13 (d)-(e), Section 3.2) ~~promoted the HONO formation from the heterogeneous reaction of NO_2 on the aerosol surface during 14:00-16:00~~. ~~On the other hand~~Contrarily, the solar radiation intensity (SRI) (~600 W/m^2) at 09:00~~-~~11:00 was obviously larger than that (~250 W/m^2) at 14:00~~-~~16:00 (Figure ~~14~~13 (f)). The higher SRI accelerated the photolysis of HONO during 09:00~~-~~11:00 period (Kraus et al., 1998). Therefore, the lower formation rate and higher photolysis rate lead~~ed~~ to a significantly lower HONO concentration at 09:00~~-~~11:00 than~~t~~ that at 14:00~~-~~16:00.

3.4.3 03 May: A typical event with unknown HONO source

The measurement ship ~~carried out~~conducted observation in the sea area near Zhanjiang on 03 May, 2018. As shown in Figure ~~15~~14, we found that there was an obvious sinking process for aerosol from ~1.0 km during 09:00~~-~~16:00, and eventually accumulated near the sea surface with a high extinction coefficient > 0.92 km^{-1}. The NO_2 was mainly concentrated near the sea surface layer (0~~-~~400 m) with an averaged concentration of 8.93 ppb from 08:00 to 09:00. ~~Afterwards~~Thereafter, with the rise the planetary boundary layer (PBL) height after sunrise, NO_2 was gradually mixed and spread throughout the PBL from 09:00~~-to-~~13:00. During this period, it was accompanied by the increase of the NO_2 concentration (averaged 11.2 ppb) under PBL (Figure ~~S7~~S14). It is due to the contribution of ship emissions near the sea surface. ~~On the other hand~~Contrarily, the regional transport of NO_2 from land also increased the NO_2 concentration in this ~~sea~~ area of the sea, with ~~the~~ wind speed ~~increase~~ increasing from 2.5 to 7.8 m/s with a north wind direction from 10:00~~-to-~~16:00 (Figure ~~15~~14 (g)).

Several HONO peaks (> 0.2 ppb) at 0.5-1.0 km were found from 09:45 to 13:00, and the aerosol and NO_2 high values were also observed at this height layer, simultaneously~~. That means, which implies that~~ the heterogeneous reaction of NO_2 on aerosol surface is more important than that on the sea surface for HONO source under sea atmosphere. ~~In~~ aAdditionally, HONO concentration obviously elevated after 14:00, especially during 14:00~~-~~16:00 (> 0.4 ppb). It ~~might~~ may be sourced from heterogeneous reaction of NO_2 on the aerosol surface, under RH a being ~92.5% (Figure ~~15~~14 (d)). The photolysis of HONO also decreased with SRI < 150 W/m^2 (Figure ~~15~~14 (f)) during this period. ~~Moreover~~Furthermore, a HONO peak (> 0.32 ppb) was observed during 16:40~~-~~17:10. However, the NO_2 concentration always kept low~~er concentration~~ (< 1.5 ppb) after 16:00, and the temperature was lower than 17 ℃ (Figure ~~15~~14 (e)), ~~and it~~which indicates the heterogeneous reaction of NO_2 ~~being~~ not being the source of ~~this~~ the observed HONO peak. The wind was north dominant with an average speed at 7.8 m/s after 15:00, which implies that ~~and it means~~ the regional transport ~~might~~ may not be the source of ~~this~~ the observed high-concentration of HONO. ~~Moreover~~Furthermore, the SRI was lower than 87.5 W/m^2, and it shows the photolysis of nitrate aerosol also ~~being~~ not being the source of the elevated HONO. The unknown HONO source in this ~~sea~~ area of the sea need to be further explored.

4 Summary and Conclusions

Currently, many uncertainties in the study of the HONO forming mechanism through the heterogeneous reaction of NO_2 exist. Earlier studies mostly focused on the near-surface layer, and the assessment of the contribution of NO_2 heterogeneous reaction to HONO formation in the vertical direction of the boundary layer is insufficient. Therefore, we aim to learn the sea-land and vertical differences of the HONO forming mechanism from NO_2 heterogeneous reaction and provide deep insights into the distribution characteristics, transforming process and environmental effects of tropospheric HONO. Ship based MAX-DOAS observations along the marginal seas of China were performed from 19 April to 16 May 2018~~,~~ ~~simultaneously~~Simultaneously, two ground~~-~~-based MAX-DOAS observations were ~~carried out~~conducted in the inland station CAMS and the coastal station SUST ~~during the same time~~ to measure the aerosol, NO_2, and HONO vertical profiles~~. to learn the sea-land and vertical differences of NO_2 heterogeneous reaction to produce HONO.~~

Along the cruise route, ~~The latitude and longitude ranges of the entire ship based campaign covered 21.12°N-35.89°N and 110.67°E-122.16°E, respectively. w~~We found five hot spots of enhanced tropospheric NO_2 ~~and HONO~~ VCDs in Yangtze River Delta, Taiwan straits, Guangzhou-Hong Kong-Macao Greater Bay areas, Zhanjiang Port, and Qingdao port. ~~The averaged values of NO_2 in above five areas were 1.07×10^{16}, 1.30×10^{16}, 7.27×10^{15}, 5.34×10^{15}, and 3.12×10^{15} molec. cm^{-2}~~Under high-level NO_2 conditions in the above five hot spots, we also observed~~,~~ enhanced HONO levels~~and the averaged HONO concentrations in above five areas were 1.01×10^{15}, 7.91×10^{14}, 6.02×10^{14}, 5.36×10^{14}, and 5.17×10^{14} molec. cm^{-2}, respectively~~. ~~However~~Contrastingly, the low-concentration HONO accompanied high-level NO_2 ~~we found NO_2 showed a higher concentration (1.66×10^{16} molec. cm^{-2}), while HONO showed a lower concentration (2.06×10^{14} molec. cm^{-2})~~ in the southeast coastline of Jiangsu province. ~~Moreover, the averaged near-surface NO_2 concentrations were 8.46 and 11.31 ppb, and the averaged near-surface HONO concentrations were 0.23 and 0.27 ppb under sea-oriented and land-oriented observation azimuths during the whole campaign, respectively.~~ When peak AOD and NO_2 conditions were observed, enhanced HONO were observed, although the reverse was not always the case.~~HONO always appeared under high AOD and NO_2 conditions.~~

~~In order t~~To ~~further~~ understand the impacts of RH, temperature, and ~~SRI~~ aerosol on the heterogeneous reaction of NO_2 to produce HONO, the emission ratios of $\Delta HONO / \Delta NO_x$ ~~in sea, inland and coastal areas~~ were calculated ~~with values of $0.46\pm0.31\%$, $0.82\pm0.34\%$, and $0.79\pm0.31\%$~~ to ~~remove~~ quantify the contribution of the primary HONO source to the total production of HONO. We found that the RH turning points in CAMS and SUST cases were both ~65% (60–70%), whereas two turning peaks (~60% and ~85%) of RH were found in the sea cases. This implied that high RH could contribute to the secondary formation of HONO in sea atmosphere. With increase in temperature, the $HONO/NO_2$ decreased with peak values appearing at ~12.5℃ in CAMS, whereas the $HONO/NO_2$ gradually increased and reached peak values at ~31.5℃ in SUST. In the sea case, when the temperature exceeded 18.0℃, the $HONO/NO_2$ increased with the increasing temperature and achieved peak at ~25.0℃. This indicated that high temperature could promote the secondary formation of HONO in the sea and coastal atmosphere. Additionally, the correlation analysis under different sea-land conditions indicated that the ground surface is more crucial to the formation of HONO from NO_2 heterogeneous reaction in the inland case, whereas the aerosol surface contributed more in the coastal and sea cases.

~~We found the RH turning points in CAMS and SUST are all ~65% (60-70%). The $HONO/NO_2$ increased with increase of RH under 65%, and the $HONO/NO_2$ decreased when RH is larger than 65%. However, two turning peaks (~60% and ~85%) of RH were found in sea case. That means high RH could contribute to the secondary formation of HONO in sea atmosphere. Moreover, the $HONO/NO_2$ decreased with the increase of temperature, and with peak values on ~12.5℃ in CAMS, however, it increase with increasing temperature, and peaked at ~31.5℃ in SUST. In sea case, the $HONO/NO_2$ increased with the increase of temperature with a peak value on ~25.0℃ under the temperature > 18.0℃, simultaneously, a ~1.9 averaged $HONO/NO_2$ high value was found under ~15.0℃. It illustrated the high temperature could promote the formation of HONO from NO_2 heterogeneous reaction in sea and coastal atmosphere. In addition, the correlation analysis under different sea-land conditions told us the ground surface plays a more important role than aerosol surface during the HONO formation from the heterogeneous reaction of NO_2 under inland case, while the aerosol surface plays a more important role during above process under coastal and sea cases.~~

Furthermore, we found that the $HONO/NO_2$ in the sea case ~~is~~ was about 4.5 times larger than that in the inland case above 600 m ~~under aerosol extinction coefficient~~ when AEC was ~0.2 km^{-1}, and the $HONO/NO_2$ ratio in the sea case ~~is~~ was about 2 times larger than that in the inland case above 600 m ~~under~~ when ~~aerosol extinction coefficient~~AEC was ~0.8 km^{-1}~~,~~ ~~which implied That~~ that means the generation rate of HONO from NO_2 heterogeneous reaction in the sea case is larger than that in the inland ~~CASE~~ case in higher atmospheric layers (~~above~~ 600 m). To have a deep understanding of three potential contributing factors of HONO production under marine condition, we selected three typical events, which represented the impacts of transport, NO_2 heterogeneous reaction and unknown HONO source, respectively.

Acknowledgements

This research is supported by the National Natural Science Foundation of China (42207113~~, U21A2027~~), the Anhui Provincial Natural Science Foundation (2108085QD180), the Presidential Foundation of the Hefei Institutes of Physical Science, Chinese Academy Sciences (YZJJ2021QN06), the National Natural Science Foundation of China (41941011, 51778596, 41575021 and 41977184), the Strategic Priority Research Program of the Chinese Academy of Sciences (XDA23020301), the National High-Resolution Earth Observation Project of China (No. 05-Y30B01-9001-19/20-3). We would like to also thank Fudan University (Professor Jianmin Chen's group) for organizing the ship-based campaign and providing meteorological data.

Compliance with ethics guidelines

All authors (the name of author) declare that they have no conflict of interest or financial conflicts to disclose.

References

[1] Alicke B, Geyer A, Hofzumahaus A, Holland F, Konrad S, Patz H W, Schafer J, Stutz J, Volz-Thomas A, Platt U. OH formation by HONO photolysis during the BERLIOZ experiment, J. Geophys. Res.-Atmos., 2003, 108, 8247.
[2] Kleffmann J, Gavriloaiei T, Hofzumahaus A, Holland F, Koppmann R, Rupp L, Schlosser E, Siese M, Wahner A. Daytime formation of nitrous acid: A major source of OH radicals in a forest, Geophys. Res. Lett., 2005, 32, L05818.
[3] Michoud V, Kukui A, Camredon M, Colomb A, Borbon A, Miet K, Aumont B, Beekmann M, Durand-Jolibois R, Perrier S, Zapf P, Siour G, Ait-Helal W, Locoge N, Sauvage S, Afif C, Gros V, Furger M, Ancellet G, Doussin J F. Radical budget analysis in a suburban European site during the MEGAPOLI summer field campaign. Atmos. Chem. Phys., 2012, 12, 11951–11974.
[4] Ryan RG, Rhodes S, Tully M, Wilson S, Jones N, Frieß U, Schofield R. Daytime HONO, NO_2 and aerosol distributions from MAX-DOAS observations in Melbourne. Atmos. Chem. Phys., 2018, 18, 13969–13985.
[5] Xue C, Zhang C, Ye C, Liu P, Catoire V, Krysztofiak G, Chen H, Ren Y, Zhao X, Wang J, Zhang F, Zhang C, Zhang J, An J, Wang T, Chen J, Kleffmann J, Mellouki A, Mu Y. HONO Budget and Its Role in Nitrate Formation in the Rural North China Plain. Environ. Sci. Technol., 2020, 54, 11048-11057.
[6] Huang R, Zhang Y, Bozzetti C, Ho K F, Cao J J, Han Y, Daellenbach K R, Slowik J G, Platt S M, Canonaco F, Zotter P, Wolf R, Pieber S M, Bruns E A, Crippa M, Ciarelli G, Piazzalunga A, Schwikowski M, Abbaszade G, Schnelle-Kreis J, Zimmermann R, An Z, Szidat S, Baltensperger U, Haddad I E, Prevot A S H. High secondary aerosol contribution to particulate pollution during haze events in China. Nature, 2014, 514, 218-222.
[7] Zhang B, Wang Y, Hao J. Simulating aerosol-radiation-cloud feedbacks on meteorology and air quality over eastern China under severe haze conditions in winter. Atmos. Chem. Phys., 2015, 15, 2387–2404.
[8] Wang L, Wen L, Xu C, Chen J, Wang X, Yang L, Wang W, Yang X, Sui X, Yao L, Zhang Q. HONO and its potential source particulate nitrite at an urban site in North China during the cold season. Sci. Total Environ., 2015, 538, 93–101.
[9] Fu X, Wang T, Zhang L, Li Q, Wang Z, Xia M, Yun H, Wang W, Yu C, Yue D, Zhou Y, Zheng J, Han R. The significant contribution of HONO to secondary pollutants during a severe winter pollution event in southern China. Atmos. Chem. Phys., 2019, 19, 1–14.
[10] Liu J, Liu Z, Ma Z, Yang S, Yao D, Zhao S, Hu B, Tang G, Sun J, Cheng M, Xu Z, Wang Y. Detailed budget analysis of HONO in Beijing, China: Implication on atmosphere oxidation capacity in polluted megacity. Atmos. Environ., 2021, 244, 117957.
[11] Yang Y, Li X, Zu K, Lian C, Chen S, Dong H, Feng M, Liu H, Liu J, Lu K, Li S, Ma X, Song D, Wang W, Yang S, Yang X, Yu X, Zhu Y, Zeng L, Tan Q, Zhang Y. Elucidating the effect of HONO on O_3 pollution by a case study in southwest China. Sci. Total Environ., 2021, 756, 144127.
[12] Zha Q, Xue L, Wang T, Xu Z, Yeung C, Louie P K K, Luk C W Y. Large conversion rates of NO_2 to HNO_2 observed in air masses from the South China Sea: Evidence of strong production at sea surface? Geophys. Res. Lett., 2014, 41, 7710–7715.
[13] Cui L, Li R, Fu H, Li Q, Zhang L, George C, Chen J. Formation features of nitrous acid in the offshore area of the East China Sea. Sci. Total Environ., 2019, 682, 138–150.
[14] Wen L, Chen T, Zheng P, Wu L, Wang X, Mellouki A, Wang W. Nitrous acid in marine boundary layer over eastern Bohai Sea, China: Characteristics, sources, and implications. Sci. Total Environ., 2019, 670, 282–291.
[15] Gil G, Kim J, Lee M, Lee G, Lee D, Jung J, An J, Hong J, Cho S, Lee J, Long R. The role of HONO in O_3 formation and insight into its formation mechanism during the KORUS-AQ Campaign. Atmos. Chem. Phys. Discus., 2019, https://doi.org/10.5194/acp-2019-1012.
[16] Cui L, Li R, Zhang Y, Meng Y, Fu H, Chen J. An observational study of nitrous acid (HONO) in Shanghai, China: The aerosol impact on HONO formation during the haze episodes. Sci. Total Environ., 2018, 630, 1057–1070.
[17] Tan W, Liu C, Wang S, Xing C, Su W, Zhang C, Xia C, Liu H, Cai Z, Liu J. Tropospheric NO_2, SO_2, and HCHO over the East China Sea, using ship-based MAX-DOAS observations and comparison with OMI and OMPS satellite data. Atmos. Chem. Phys., 2018, 18, 15387–15402.
[18] Zhang W, Tong S, Jia C, Wang L, Liu B, Tang G, Ji D, Hu B, Liu Z, Li W, Wang Z, Liu Y, Wang Y, Ge M. Different HONO Sources for Three Layers at the Urban Area of Beijing. Environ. Sci. Technol., 2020, 54, 12870-12880.

[19] Cheng P, Cheng Y, Lu K, Su H, Yang Q, Zou Y, Zhao Y, Dong H, Zeng L, Zhang Y. An online monitoring system for atmospheric nitrous acid (HONO) based on stripping coil and ion chromatography. J. Environ. Sci., 2013, 25(5) 895–907.
[20] Bernard F, Cazaunau M, Grosselin B, Zhou B, Zheng J, Liang P, Zhang Y, Ye X, Daele V, Mu Y, Zhang R, Chen J, Mellouki A. Measurements of nitrous acid (HONO) in urban area of Shanghai, China. Environ. Sci. Pollut. Res., 2016, 23:5818–5829.
[21] Jordan N, Osthoff HD. Quantification of nitrous acid (HONO) and nitrogen dioxide (NO_2) in ambient air by broadband cavity-enhanced absorption spectroscopy (IBBCEAS) between 361 and 388 nm. Atmos. Meas. Tech., 2020, 13, 273–285.
[22] Guo Y, Wang S, Gao S, Zhang R, Zhu J, Zhou B. Influence of ship direct emission on HONO sources in channel environment. Atmos. Environ., 2020, 242, 117819.
[23] Meng F, Qin M, Tang K, Duan J., Fang W., Liang S., Ye K., Xie P., Sun Y., Xie C., Ye C., Fu P., Liu J., Liu W. High-resolution vertical distribution and sources of HONO and NO_2 in the nocturnal boundary layer in urban Beijing, China. Atmos. Chem. Phys., 2020, 20, 5071–5092.
[24] Garcia-Nieto D, Benavent N, Saiz-Lopez A. Measurements of atmospheric HONO vertical distribution and temporal evolution in Madrid (Spain) using the MAX-DOAS technique. Sci. Total Environ., 2018, 643, 957–966.
[25] Wang Y, Dörner S, Donner S, Bohnke S, Smedt I D, Dickerson R R, Dong Z, He H, Li Z, Li Z, Li D, Liu D, Ren X, Theys N, Wang Y, Wang Y, Wang Z, Xu H, Xu J, Wagner T. Vertical profiles of NO_2, SO_2, HONO, HCHO, CHOCHO and aerosols derived from MAX-DOAS measurements at a rural site in the central western North China Plain and their relation to emission sources and effects of regional transport. Atmos. Chem. Phys., 2019, 19, 5417–5449.
[26] Xing C, Liu C, Wang S, Chan K L, Gao Y, Huang X, Su W, Zhang C, Dong Y, Fan G, Zhang T, Chen Z, Hu Q, Su H, Xie Z, Liu J. Observations of the vertical distributions of summertime atmospheric pollutants and the corresponding ozone production in Shanghai, China. Atmos. Chem. Phys. 2017, 17, 14275–14289.
[27] Xing C, Li C, Wang S, Hu Q, Liu H, Tan W, Zhang W, Li B, Liu J. A new method to determine the aerosol optical properties from multiple-wavelength O_4 absorptions by MAX-DOAS observation. Atmos. Meas. Tech., 2019, 12, 3289–3302.
[28] Xing C, Liu C, Hu Q, Fu Q, Lin H, Wang S, Su W, Wang W, Javed Z, Liu J. Identifying the wintertime sources of volatile organic compounds (VOCs) from MAX-DOAS measured formaldehyde and glyoxal in Chongqing, southwest China. Sci. Total Environ., 2020, 715, 136258.
[29] Vandaele AC, Hermans C, Simon PC, Carleer M, Colin R, Fally S, Merienne M F, Jenouvrier A, Coquart B. Measurements of the NO_2 absorption cross-section from 42,000 cm^{-1} to 10,000 cm^{-1} (238–1000 nm) at 220K and 294 K. J. Quant. Spectrosc. Ra., 1998, 59, 171–184.
[30] Serdyuchenko A, Gorshelev V, Weber M, Chehade W, Burrows J P. High spectral resolution ozone absorption cross-sections –part 2: temperature dependence. Atmos. Meas. Tech., 2014, 7, 625–636.
[31] Thalman R, Volkamer R. Temperature dependent absorption cross-sections of O_2–O_2 collision pairs between 340 and 630 nm and at atmospherically relevant pressure. Phys. Chem. Chem. Phys., 2013, 15, 15371–15381.
[32] Meller R, Moortgat GK. Temperature dependence of the absorption cross sections of formaldehyde between 223 and 323 K in the wavelength range 225–375 nm. J. Geophys. Res., 2000, 105, 7089–7101.
[33] Rothman L, Gordon I, Barber R, Dothe H, Gamache R R, Goldman A, Perevalov, Tashkun S A, Tennyson J. HITEMP, the high-temperature molecular spectroscopic database. J. Quant. Spectrosc. Ra., 2010, 111, 2139–2150.
[34] Fleischmann OC, Hartmann M, Burrows JP, Orphal J. New ultraviolet absorption cross-sections of BrO at atmospheric temperatures measured by time-windowing Fourier transform spectroscopy. J. Photoch. Photobio., 2004, A 168, 117–132.
[35] Stutz J, Kim ES, Platt U, Bruno P, Perrino C, Febo A. UV–visible absorption cross sections of nitrous acid. J. Geophys. Res.-Atmos., 2000, 105, 14585–14592.
[36] Aliwell S, Van Roozendael M, Johnston P, Richter A, Wagner T, Arlander D W, Burrows J P, Fish D J, Jones R L, Tornkvist K K, Lambert J C, Pfeilsticker K, Pundt I. Analysis for BrO in zenith-sky spectra: an Intercomparison exercise for analysis improvement. J. Geophys. Res., 2002, 107, 4199.
[37] Liu C, Xing C, Hu Q, Li Q, Liu H, Hong Q, Tan W, Ji X, Lin H, Lu C, Lin J, Liu H, Wei S, Chen J, Yang K, Wang S, Liu T, Chen Y. Ground-based hyperspectral stereoscopic remote sensing network: A promising strategy to learn coordinated control of O_3 and $PM_{2.5}$ over China. Engineering, 2021.
[38] Liu Y, Nie W, Xu Z, Wang T, Wang R, Li Y, Wang L, Chi X, Ding A. Semi-quantitative understanding of source contribution to nitrous acid (HONO) based on 1 year of continuous observation at the SORPES station in eastern China. Atmos. Chem. Phys., 2019, 19, 13289–13308.
[39] Sun L, Chen T, Jiang Y, Zhou Y, Sheng L, Lin J, Li J, Dong C, Wang C, Wang X, Zhang Q, Wang W, Xue L. Ship emission of nitrous acid (HONO) and its impacts on the marine atmospheric oxidation chemistry. Sci. Total Environ., 2020, 735, 139355.
[40] Huang R, Yang L, Cao J, Wang Q, Tie X, Ho K F, Shen Z, Zhang R, Li G, Zhu C, Zhang N, Dai W, Zhou J, Liu S, Chen Y, Chen J, O'Dowd C D. Concentration and sources of atmospheric nitrous acid (HONO) at an urban site in Western China. Sci. Total Environ., 2017, 593–594, 165–172.

[41] Xu Z, Wang T, Wu J, Xue L, Chan J, Zha Q, Zhou S, Louie P K K, Luk C W Y. Nitrous acid (HONO) in a polluted subtropical atmosphere: Seasonal variability, direct vehicle emissions and heterogeneous production at ground surface, Atmos. Environ., 2015, 106, 100–109.
[42] Xing C, Liu C, Hu Q, Fu Q, Wang S, Lin H, Zhu Y, Wang S, Wang W, Javed Z, Ji X, Liu J. Vertical distributions of wintertime atmospheric nitrogenous compounds and the corresponding OH radicals production in Leshan, southwest China. J. Environ. Sci., 2021, 105, 44–55.
[43] Song Y, Xing C, Liu C, Lin J, Wu H, Liu T, Lin H, Zhang C, Tan W, Ji X, Liu H, Li Q. Evaluation of transport processes over North China Plain and Yangtze River Delta using MAX-DOAS observations. 10.5194/egusphere-2022-653.
[44] Kleffmann J, Kurtenbach R, Lorzer J, Wiesen P, Kalthoff N, Vogel B, Vogel H. Measured and simulated vertical profiles of nitrous acid-Part I: Field measurements, Atmos. Environ., 2003, 37, 2949-2955.
[45] Stemmler K, Ammann M, Donders C, Kleffmann J, George C. Photosensitized reduction of nitrogen dioxide on humic acid as a source of nitrous acid, nature, 2006, 440, 195-198.
[46] Indarto A. Heterogeneous reactions of HONO formation from NO_2 and HNO_3: a review, 2012, 38, 1029-1041.
[47] Wang Y, Apituley A, Bais A, Beirle S, Benavent N, Borovski A, Bruchkouski H, Chan K L, Donner S, Drosoglou T, Finkenzeller H, Friedrich M M, Frieß U, Garcia-Nieto D, Gómez-Martín, L, Hendrick F, Hilboll A, Jin J, Johnston P, Koenig T K, Kreher K, Kumar V, Kyuberis A, Lampel J, Liu C, Liu H, Ma J, Polyansky O L, Postylyakov O, Querel R, Saiz-Lopez A, Schmitt S, Tian X, Tirpitz J-L, Roozendael M V, Volkamer R, Wang Z, Xie P, Xing C, Xu J, Yela M, Zhang C, Wagner T. Inter-comparison of MAX-DOAS measurements of tropospheric HONO slant column densities and vertical profiles during the CINDI-2 campaign, Atmos. Meas. Tech., 2020, 13, 5087-5116.
[48] Xu S, Wang S, Xia M, Lin H, Xing C, Ji X, Su W, Tan W, Liu C, Hu Q. Observations by ground-based MAX-DOAS of the vertical characters of winter pollution and the influencing factors of HONO generation in Shanghai, China, Remote Sens., 2021, 13(17), 3518.
[49] He S, Wang S, Zhang S, Zhu J, Sun Z, Xue R, Zhou B. Vertical distributions of atmospheric HONO and the corresponding OH radical production by photolysis at the suburb area of Shanghai, China, Sci. Total Environ., 2023, 858, 159703.
[50] Zhang N, Zhou X, Shepson P B, Gao H, Alaghmand M, Stirm B. Aircraft measurement of HONO vertical profiles over a forested region, Geophys. Res. Lett., 2009, 36(15), L15820.
[51] Wong K W, Tsai C, Lefer B, Haman C, Grossberg N, Brune W H, Ren X, Luke W, Stutz J. Daytime HONO vertical gradients during SHARP 2009 in Houston, TX, Atmos. Chem. Phys., 2012, 12, 635-652.
[52] Salgado, M. S. and Rossi, M. J.: Flame soot generated under controlled combustion conditions: Heterogeneous reaction of NO2 on hexane soot, International Journal of Chemical Kinetics, 34, 620-631, 10.1002/kin.10091, 2002.
[53] Zhou, X., Zhang, N., TerAvest, M., Tang, D., Hou, J., Bertman, S., Alaghmand, M., Shepson, P. B., Carroll, M. A., Griffith, S., Dusanter, S., and Stevens, P. S.: Nitric acid photolysis on forest canopy surface as a source for tropospheric nitrous acid, Nature Geoscience, 4, 440-443, 10.1038/ngeo1164, 2011.
[54] Kraus, A., Hofzumahaus, A. Field Measurements of Atmospheric Photolysis Frequencies for O_3, NO_2, HCHO, CH_3CHO, H_2O_2, and HONO by UV Spectroradiometry. In: Rudolph, J., Koppmann, R. (eds) Atmospheric Measurements during POPCORN — Characterisation of the Photochemistry over a Rural Area. Springer, Dordrecht. https://doi.org/10.1007/978-94-017-0813-5_8.
[55] Liu, Y., Nie, W., Xu, Z., Wang, T., Wang, R., Li, Y., Wang, L., Chi, X., and Ding, A.: Contributions of different sources to nitrous acid (HONO) at the SORPES station in eastern China: results from one-year continuous observation. , Atmospheric Chemistry and Physics Discussions, 10.5194/acp-2019-219, 2019.
[56] Rodgers, C. D., Taylor, F. W. (Ed.): Inverse methods for atmospheric sounding, theory and practice, World Scientific, 255 pp.2004.
[57] Stutz, J., Kim, E. S., Platt, U., Bruno, P., Perrino, C., and Febo, A.: UV-visible absorption cross sections of nitrous acid, Journal of Geophysical Research: Atmospheres, 105, 14585-14592, 10.1029/2000jd900003, 2000.
[58] Wang, Y., Apituley, A., Bais, A., Beirle, S., Benavent, N., Borovski, A., Bruchkouski, I., Chan, K. L., Donner, S., Drosoglou, T., Finkenzeller, H., Friedrich, M. M., Frieß, U., Garcia-Nieto, D., Gómez-Martín, L., Hendrick, F., Hilboll, A., Jin, J., Johnston, P., Koenig, T. K., Kreher, K., Kumar, V., Kyuberis, A., Lampel, J., Liu, C., Liu, H., Ma, J., Polyansky, O. L., Postylyakov, O., Querel, R., Saiz-Lopez, A., Schmitt, S., Tian, X., Tirpitz, J.-L., Van Roozendael, M., Volkamer, R., Wang, Z., Xie, P., Xing, C., Xu, J., Yela, M., Zhang, C., and Wagner, T.: Inter-comparison of MAX-DOAS measurements of tropospheric HONO slant column densities and vertical profiles during the CINDI-2 campaign, Atmospheric Measurement Techniques, 13, 5087-5116, 10.5194/amt-13-5087-2020, 2020.
[59] Wang, Y., Lampel, J., Xie, P., Beirle, S., Li, A., Wu, D., and Wagner, T.: Ground-based MAX-DOAS observations of tropospheric aerosols, NO2, SO2 and HCHO in Wuxi, China, from 2011 to 2014, Atmospheric Chemistry and Physics, 17, 2189-2215, 10.5194/acp-17-2189-2017, 2017.

720 **Table 1. Detailed information of the measurement cruise**

Cruise NO.	Periods	Measurement cruise
NO. 1	08:50 to 21:02 19 Apr.	Daishan port (30.24°N, 122.16°E) to Chongming (31.18°N, 121.82°E)
NO. 2	05:40 to 17:45 20 Apr.	Sailing around Chongming island
NO. 3	06:03 21 Apr. to 08:07 03 May	Chongming (31.18°N, 121.82°E) to Zhanjiang port (21.12°N, 110.67°E)
NO. 4	08:07 03 May to 06:52 09 May	Zhanjiang port (21.12°N, 110.67°E) to Daishan port (30.24°N, 122.16°E)
NO. 5	05:40 11 May to 05:55 14 May	Daishan port (30.24°N, 122.16°E) to Qingdao (35.89°N, 120.87°E)
NO. 6	05:55 14 May to 10:00 16 May	Qingdao (35.89°N, 120.87°E) to Daishan port (30.24°N, 122.16°E)

721

722 **Table 2. Detailed retrieval settings of O_4, NO_2 and HONO.**

Parameter	Data source	Fitting internals (nm)		
		O_4	NO_2	HONO
Wavelength range		338-370	338-370	335-373
NO_2	298K, I_0-corrected, Vandaele et al. (1998)	√	√	√
NO_2	220K, I_0-corrected, Vandaele et al. (1998)	√	√	√
O_3	223K, I_0-corrected, Serdyuchenko et al. (2014)	√	√	√
O_3	243K, I_0-corrected, Serdyuchenko et al. (2014)	√	√	√
O_4	293K, Thalman and Volkamer (2013)	√	√	√
HCHO	298K, Meller and Moortgat (2013)	√	√	√
H_2O	HITEMP (Rothman et al. 2010)	×	×	√
BrO	223K, Fleischmann et al. (2004)	√	√	√
HONO	296K, Stutz et al. (2000)	×	×	√
Ring	Calculated with QDOAS	√	√	√
Polynomial degree		Order 5	Order 5	Order 5
Intensity offset		Constant	Constant	Constant

723 * Solar I_0 correction; Aliwell et al. (2002).
724

725

726 **Table 3.** Error budget estimation (in %) of the retrieved near-surface (0-200 m) trace gas concentrations and AECs,
727 and trace gas VCDs and AOD.

			Error source				Total
			Smoothing and noise errors	Algorithm error	Cross section error	Related to the aerosol retrieval (only for trace gases)	
Cruise route	Near-surface	aerosol	14	4	4	-	15
		NO_2	16	3	3	15	22
		HONO	20	20	5	15	32
	VCD or AOD	AOD	5	8	4	-	10
		NO_2	17	11	3	10	23
		HONO	22	20	5	10	32
SUST	Near-surface	aerosol	13	4	4	-	14
		NO_2	14	3	3	14	20
		HONO	18	20	5	14	31
	VCD or AOD	AOD	5	8	4	-	10
		NO_2	16	11	3	10	22
		HONO	20	20	5	10	30
CAMS	Near-surface	aerosol	13	4	4	-	14
		NO_2	15	3	3	14	21
		HONO	19	20	5	14	31
	VCD or AOD	AOD	5	8	4	-	10
		NO_2	17	11	3	10	23
		HONO	21	20	5	10	31

728

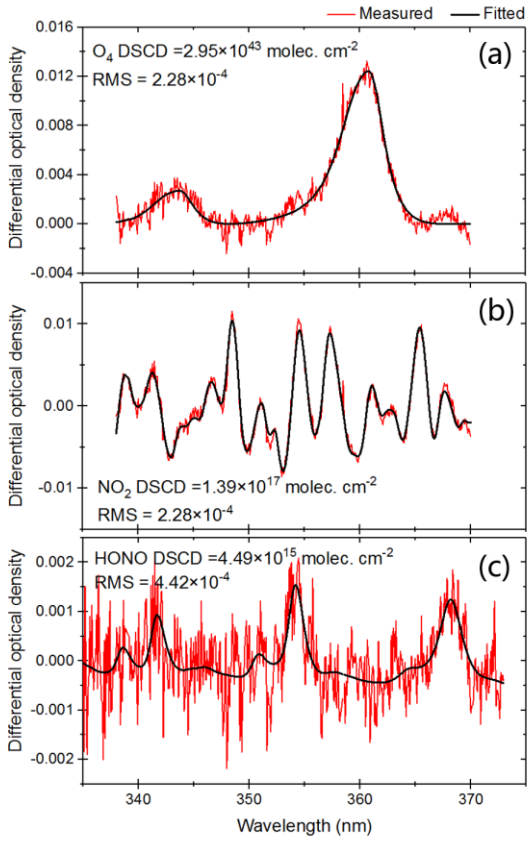

Figure 1. Typical DOAS spectral fittings for (a) O_4, (b) NO_2 and (c) HONO.

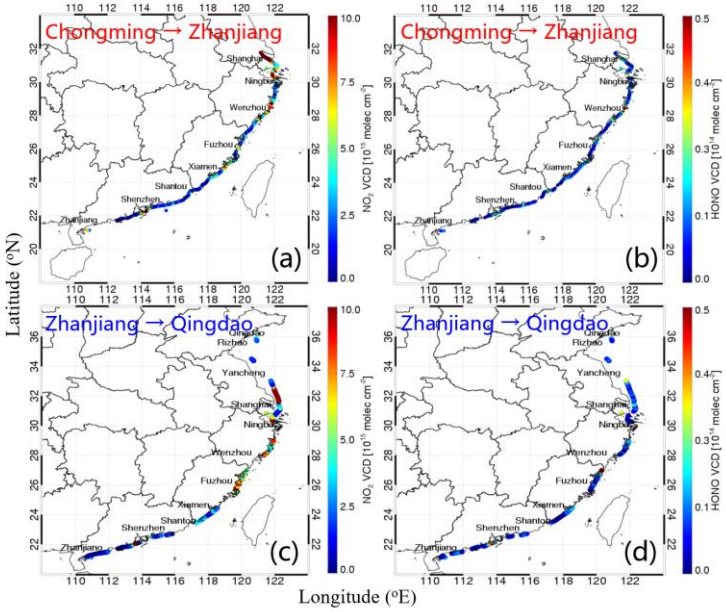

Figure 2. The spatial distributions of NO_2 and HONO VCDs. (a) and (b) show the NO_2 and HONO VCDs along the cruise route from Chongming to Zhanjiang. (c) and (d) depict the NO_2 and HONO VCDs along the cruise route from Zhanjiang to Qingdao.

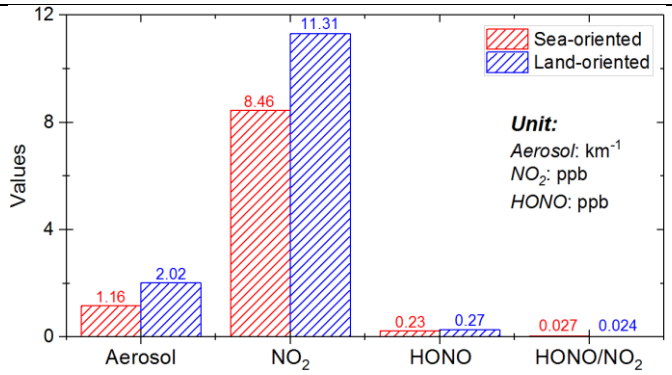

Figure 3. Averaged aerosol extinction, NO_2 concentration, HONO concentration and HONO/NO_2 ratio during the campaign. The red and blue boxes denoted sea-oriented and land-oriented measurements, respectively.

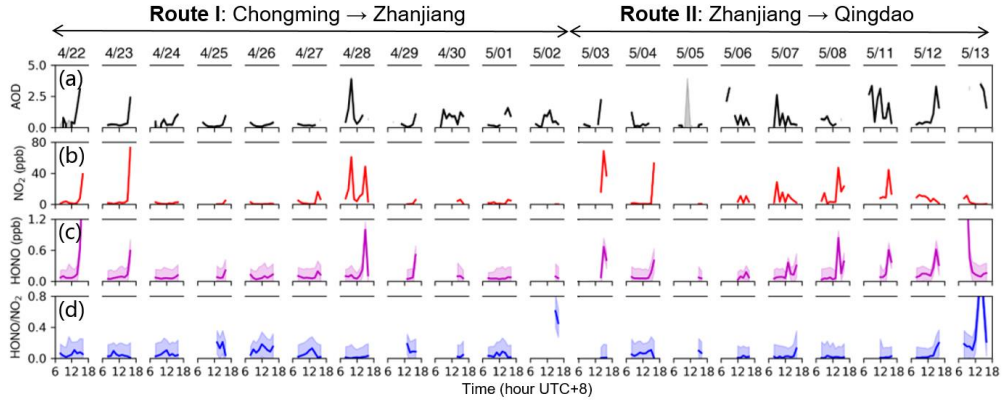

Figure 4. Time series of (a) AOD, (b) surface NO_2 concentration, (c) surface HONO concentration, and (f) surface HONO/NO_2 ratios.

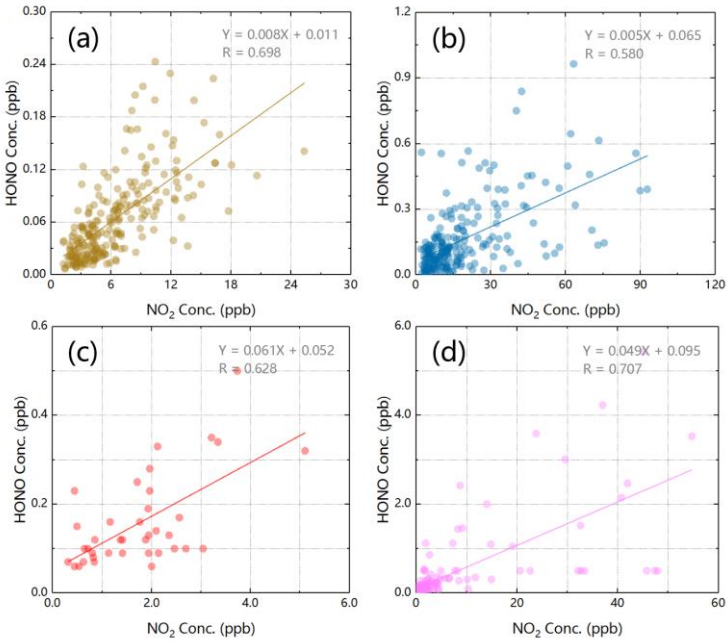

Figure 5. Linear regression plots between surface NO_2 and HONO concentrations in (a) CAMS, (b) SUST, and ship-based measurements of (c) sea-oriented and (d) land-oriented under static weather condition.

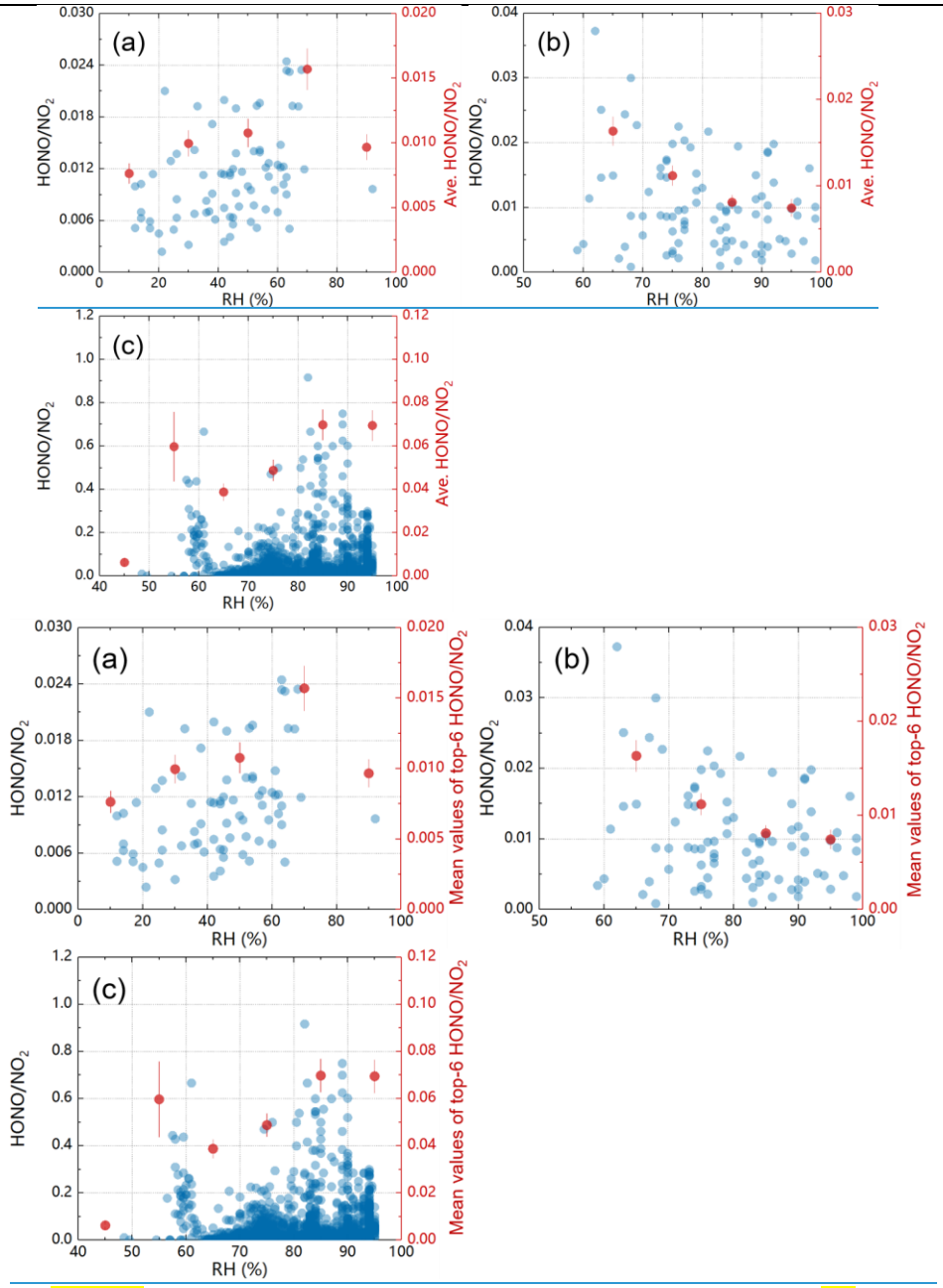

Figure 6. Scatter plots between RH and $HONO/NO_2$ ratios in (a) CAMS, (b) SUST, and (c) the ship-based campaign.

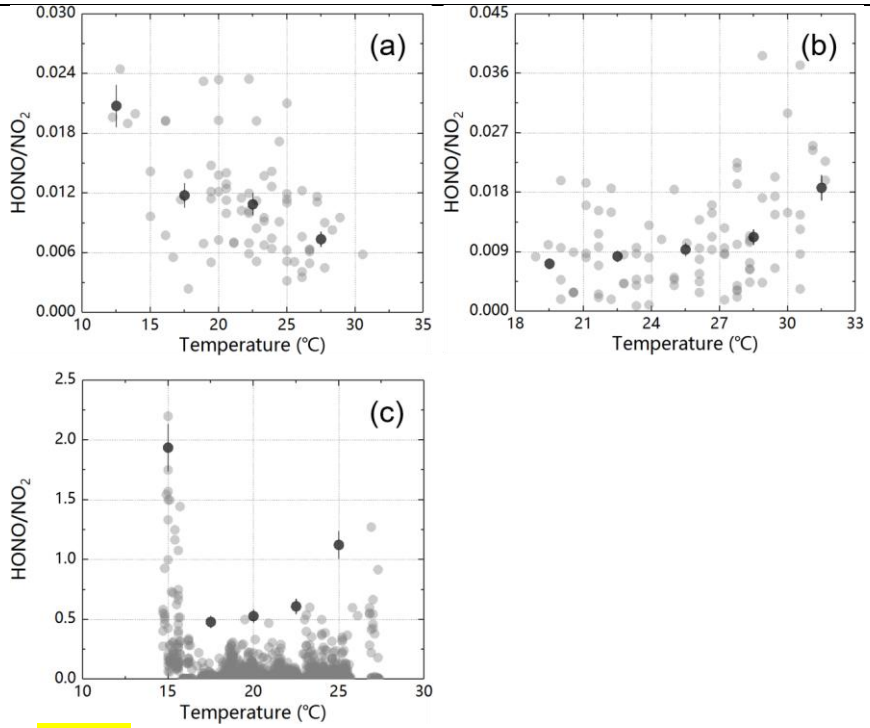

Figure 7. Scatter plots between temperature and HONO/NO_2 ratios in (a) CAMS, (b) SUST, and (c) the ship-based campaign.

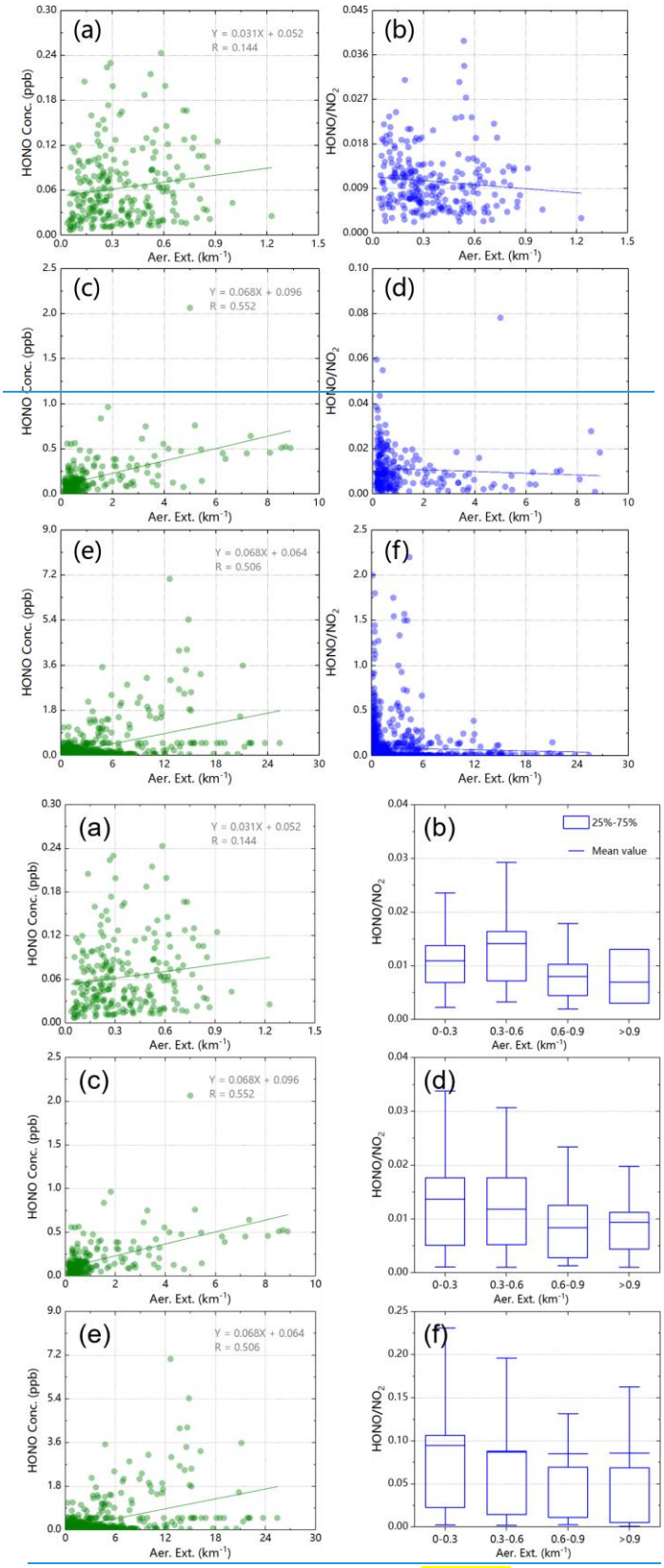

Figure 8. (a), (c) and (e) showed the linear regression plots between surface aerosol extinction and HONO concentrations in CAMS, SUST and the ship-based campaign, respectively. (b), (d) and (f) depicted the ~~scatter plots~~$HONO/NO_2$ ratio distribution under different aerosol extinction coefficient conditions ~~between surface aerosol extinction and $HONO/NO_2$ ratios~~ in CAMS, SUST and the ship-based campaign.

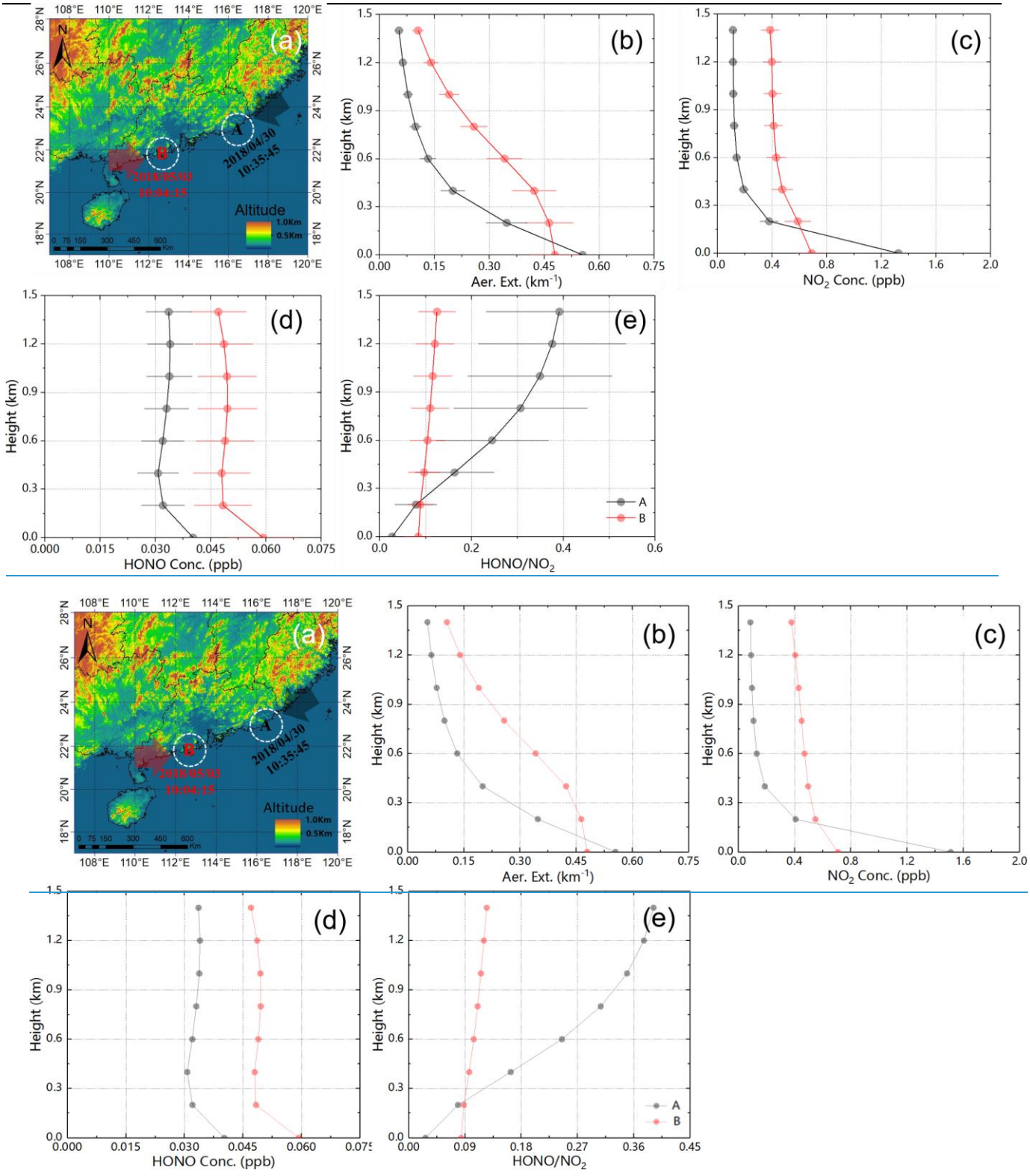

Figure 9. (a) showed two measurement points (A: black, sea-oriented with sea wind; B: red, land-oriented with land wind) during the campaign. (b)-(e) showed the vertical profiles of aerosol, NO_2, HONO, and HONO/NO_2 ratios in above two measurement points, respectively.

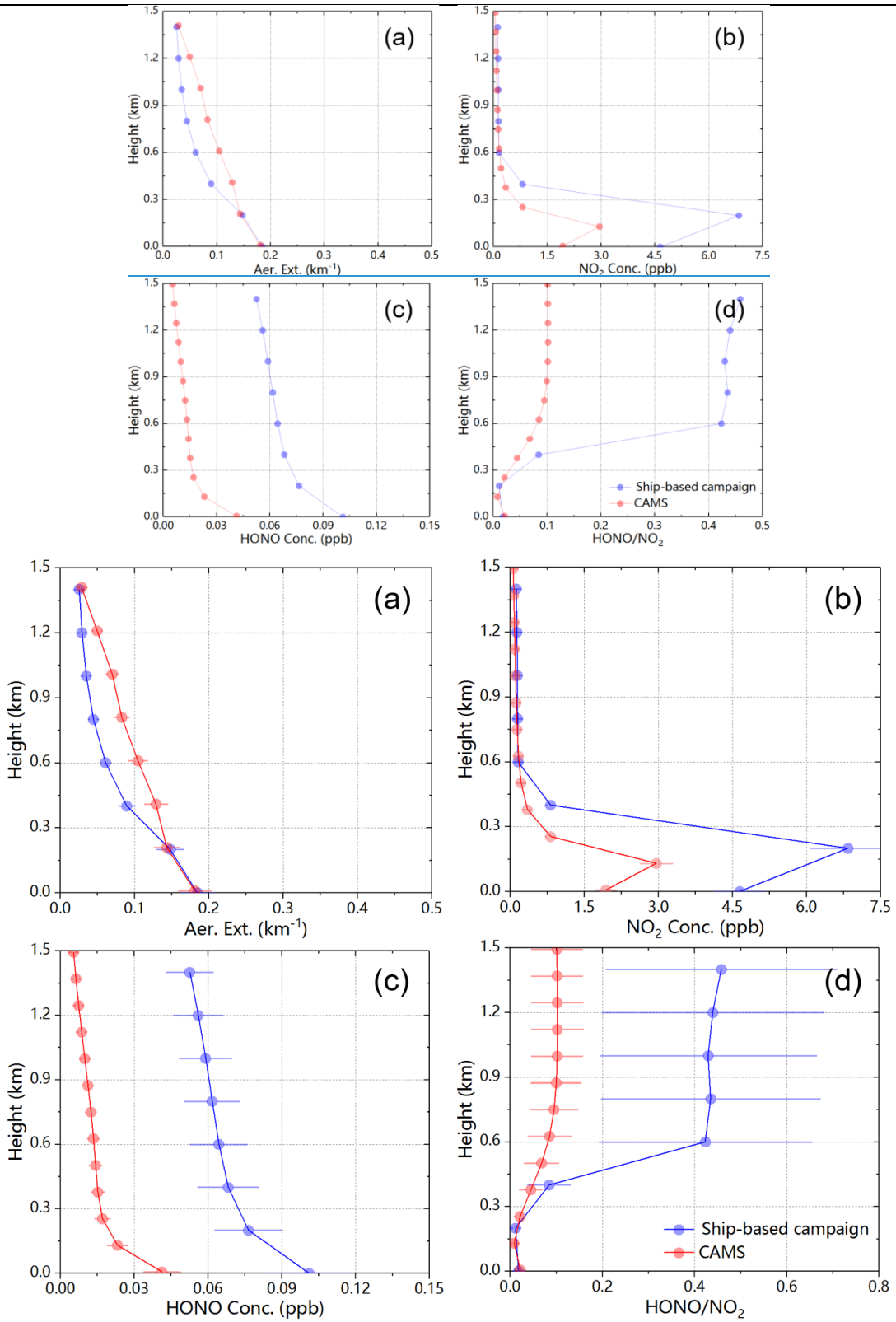

Figure 10. Vertical distributions of (a) aerosol extinction, (b) NO_2 concentration, (c) HONO concentration, and (d) HONO/NO_2 ratio. The blue and red lines represented a ship-based campaign case and a CAMS ~~inland~~ case, respectively.

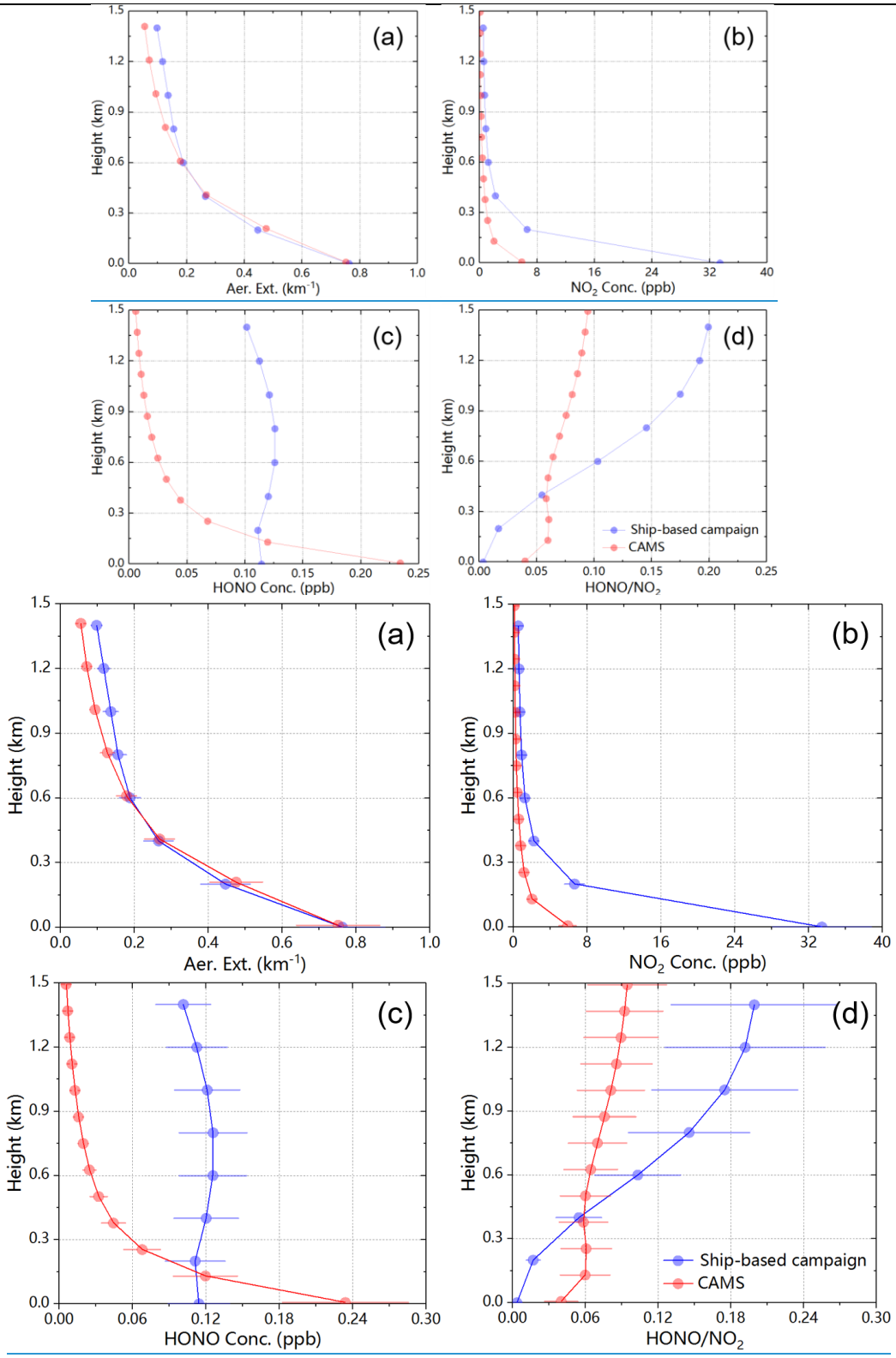

Figure 11. Vertical distributions of (a) aerosol extinction, (b) NO_2 concentration, (c) HONO concentration, and (d) HONO/NO_2 ratio. The blue and red lines represented a ship-based campaign case and a CAMS ~~inland~~ case, respectively.

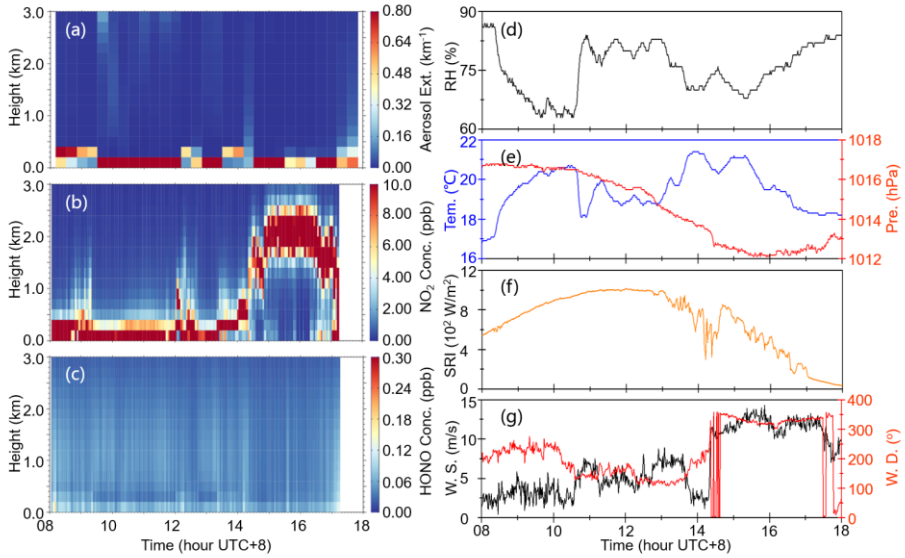

Figure 12. Case of 20 April 2018. Time series of (a) aerosol extinction, (b) NO_2 and (c) HONO vertical profiles, respectively. (d) showed the time series of surface RH. (e) depicted the time series of surface temperature and pressure. (f) showed the time series of surface SRI. (g) depicted the time series of surface wind speed and wind direction.

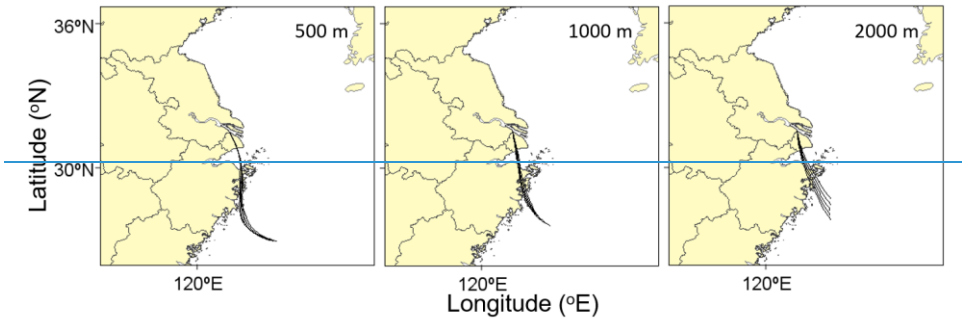

~~Figure 13. Daily 24-h backward trajectories of air masses at (a) 500 m, (b) 1000 m, and (c) 2000 m on 20 April 2018, respectively.~~

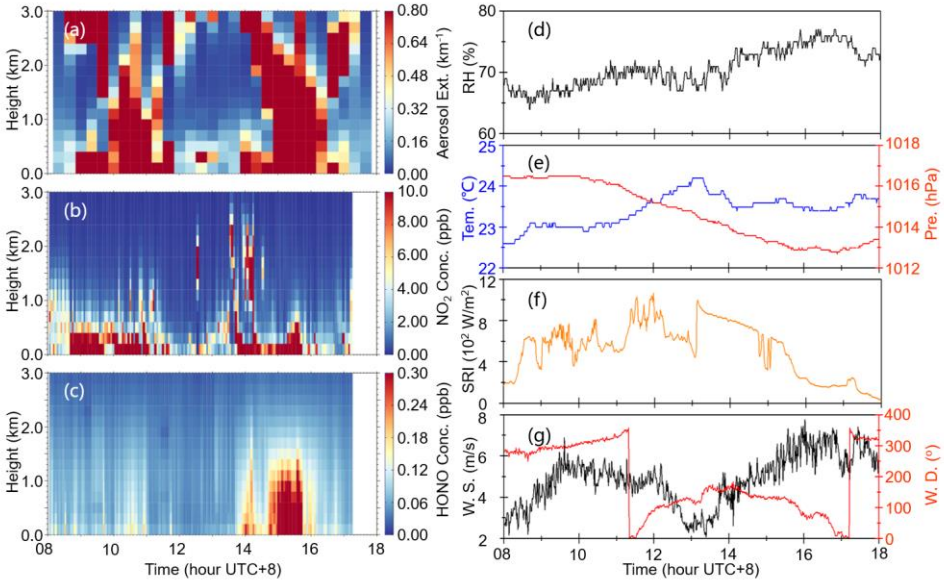

Figure 14. Case of 28 April 2018. Time series of (a) aerosol extinction, (b) NO_2 and (c) HONO vertical profiles, respectively. (d) showed the time series of surface RH. (e) depicted the time series of surface temperature and

pressure. (f) showed the time series of surface SRI. (g) depicted the time series of surface wind speed and wind direction.

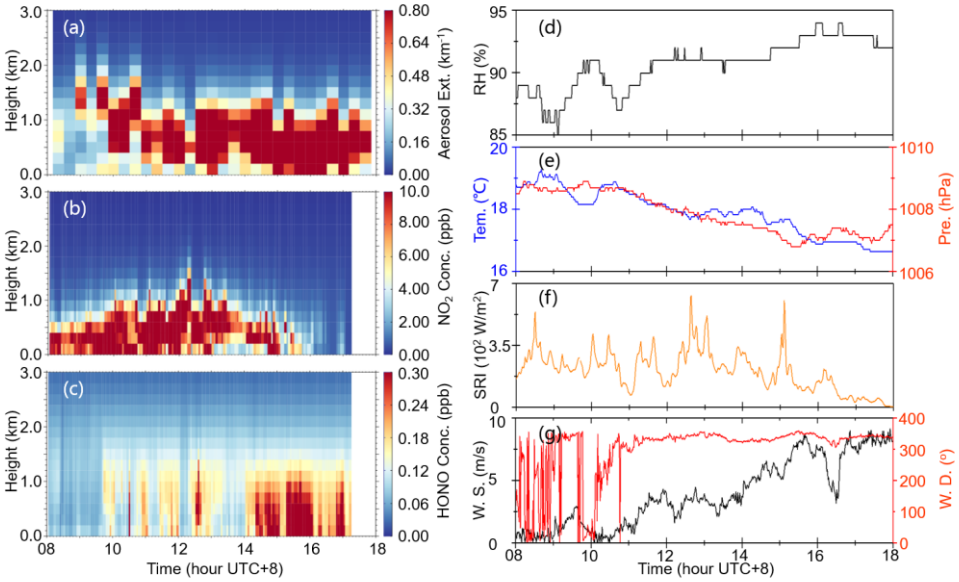

Figure 15. Case of 03 May 2018. Time series of (a) aerosol extinction, (b) NO_2 and (c) HONO vertical profiles, respectively. (d) showed the time series of surface RH. (e) depicted the time series of surface temperature and pressure. (f) showed the time series of surface SRI. (g) depicted the time series of surface wind speed and wind direction.